Generalizable Framework of Unpaired Domain Transfer and Deep Learning for the Processing of Real-Time Synchrotron-Based X-Ray Microcomputed Tomography Images of Complex Structures

Kunning Tang, Ying Da Wang, James McClure, Cheng Chen, Peyman Mostaghimi, and Ryan T. Armstrong

Phys. Rev. Applied **17**, 034048 — Published 17 March 2022

DOI: 10.1103/PhysRevApplied.17.034048

Generalizable framework of unpaired domain transfer and deep learning for the processing of real-time synchrotron-based X-ray microcomputed tomography images of complex structures

Kunning Tang[a], Ying Da Wang[a], James McClure[b], Cheng Chen[c], Peyman Mostaghimi[a], Ryan T. Armstrong[a]

[a] School of Minerals and Energy Resources Engineering, The University of New South Wales, NSW 2052, Australia
[b] Advanced Research Computing, Virginia Tech, Blacksburg, VA, USA.
[c] Department of Mining and Minerals Engineering, Virginia Tech, Blacksburg, VA, USA

Correspondence to:
Kunning Tang
z5189000@ad.unsw.edu.au
https://orcid.org/0000-0002-3584-3097

Abstract

Mitigating greenhouse gas emissions by underground carbon dioxide storage or by coupling intermittent renewable energy with underground hydrogen storage are solutions essential to the future of energy. Of particular importance to the success of underground storage is the fundamental understanding of geochemical reactions with mineralogical phases and flow behavior at the length scale at which interfaces are well resolved. Fast synchrotron-based three-dimensional (3D) X-ray micro-computed tomography (μ-CT) of rocks is a widely used technique that provides real-time visualization of fluid flow and transport mechanisms. However, fast imaging results in significant noise and artifacts that complicate the extraction of quantitative data beyond the basic identification of solid and void regions. To address this issue, an image-processing workflow is introduced that begins with unpaired domain transfer by CycleGAN, which is used to transfer synchrotron-based micro-CT images containing fast-imaging-associated noise to long-scan, high-quality μ-CT images that have paired ground truth labels for all phases. The second part of the workflow is multi-mineral segmentation of images using convolutional neural networks (CNNs). Four CNNs were trained using the transferred dynamic-style μ-CT images. A quantitative assessment of physically meaningful parameters and material properties is carried out. In terms of physical accuracy, the results show a high variance for each network output, which indicates that the segmentation performance cannot be fully revealed by pixelwise accuracy alone. Overall, the integration of unpaired domain transfer with CNN-based multi-mineral segmentation provides a generalizable digital material framework to study the physics of porous materials for energy-related applications, such as underground CO_2 and H_2 storage.

Keywords

Real-time μ-CT imaging; Deep learning; Image domain transfer; Multi-mineral segmentation; Physical analysis; Mixed-wetting flow simulation.

1. Introduction

The adoption of the Paris Agreement in 2015 renewed enthusiasm toward greenhouse gas emission mitigation and the transition from fossil fuels to renewable-energy-based systems [1–3]. The capture and geological storage of emitted CO_2 (CCS) is a promising method for reducing atmospheric greenhouse gas, and underground hydrogen storage (UHS), which stores excess renewable energy in the form of hydrogen in geological structures, is an emerging means of resolving renewable energy intermittency [4–8]. When it comes to the research regarding containment, capillary trapping and hydrogen loss are two key factors that determine the feasibility of CCS and UHS. The performance of CO_2 capillary trapping significantly depends on the wettability of the surrounding minerals [9,8], and hydrogen loss is mainly controlled by the mineral types and their dissolution and precipitation processes [10–12]. Therefore, understanding reservoir rock mineralogy and the corresponding flow behavior is essential for deciphering the CO_2 and H_2 storage efficiencies.

With the aid of digital rock physics (DRP), rock mineralogy and flow dynamics can be characterized comprehensively on the length scale at which interfaces are well resolved [13,14,10,15]. The workflow for DRP provides a generalizable technique for mineralization and flow analyses in complex micrometer-sized structures, which starts with image acquisition, image processing, and subsequent physical measures and/or numerical simulation of flow and transport mechanisms [16,17,17,18,13,19]. To date, the focus has extended from static to dynamic analysis, such as dynamic image acquisition by synchrotron-based X-ray micro-computed tomography (μ-CT), which provides 3D real-time images of fluid flow and transport phenomena in porous media [20,21]. This dynamic imaging technique can be potentially used to capture the dynamics of CO_2 and H_2 distribution, flow behavior, and reaction with minerals in porous rocks. However, the fast acquisition time results in a relatively low-intensity signal in comparison to standard imaging techniques, where acquisition times are an order of magnitude greater. The low signal-to-noise ratio results in images that are challenging to process, especially for image segmentation. Therefore, these images are segmented into void and solid phases; however, for many physical processes, the actual distribution of the constitutive minerals and their interactions with the flowing fluids are important. With multiphase flow, the varying mineralogy and associated wetting properties are important. Thus, without the development of an image processing workflow for dynamic data, it is challenging to capture accurate pore structures for the simulation of physical processes within a digital framework.

3D μ-CT is a non-invasive and non-destructive imaging tool that has been used to capture rock features and fluid/gas distributions to support compositional characterization, pore network modeling, and the assessment of mineralogy and other petrophysical parameters [22–25]. Numerical simulations of fluid flow at the pore scale, such as multi-mineral reactive transport and single-phase and two-phase flow, can be directly performed on μ-CT images, which are highly related to underground CO_2 and H_2 storage [26,27]. Several studies have substantiated that numerical simulations of 3D μ-CT images reasonably agree with experimental results [28–31]. However, several hours are required to obtain high-quality 3D μ-CT images, which limits their utilization for the imaging of dynamic processes [32,33]. Important fundamental scientific questions remain regarding the role of transient processes during multiphase flow [20,34]. To address these issues, synchrotron-based μ-CT imaging has attracted attention owing to its extremely high photon flux, which makes it possible to capture full 3D images within seconds [35]. Therefore, real-time 3D dynamic imaging can be achieved with synchrotron-based μ-CT [20] but at the expense of image quality [36].

Accurate feature characterization and flow simulation of μ-CT images rely on image segmentation. Image segmentation in DRP refers to the process of partitioning μ-CT images into multiple mineral phases, pores, and fluid/gas phases [18]. To date, several studies have performed μ-CT image segmentation by proposing machine-learning methods, especially the use of advanced convolutional neural networks (CNNs) [37–41]. A CNN is built within a deep learning framework that performs multiphase segmentation with the benefit of eliminating user judgment of the parameters associated with segmentation. CNNs can capture informative features and semantics from images with receptive fields by stacking several convolutional layers with nonlinearities and down-sampling layers. CNNs have been widely used in the field of computer vision, including object detection [42], image classification [43,44], super-resolution [45], image-to-image translation [46] and image segmentation [47,48]. In regards to CNN-based semantic segmentation, compared to traditional segmentation techniques including edge detection methods, thresholding methods, or region-based methods, CNN relies less on the voxel intensity frequency distribution and reduces the requirement of expert intervention [49,50]. A study of segmentation with both a watershed segmentation technique and CNN methods demonstrated that CNN gives a better segmentation result in terms of phase boundaries and connectivity [51],. A study of dual-energy X-ray absorptiometry images to distinguish between bone and soft tissue compared the segmentation accuracy between Otsu's thresholding and a deep learning method [52]. The pixel-based accuracy using deep learning was significantly higher than Otsu's thresholding method. These results suggest that CNNs have matured to the point that they outperform other methods for semantic segmentation [52–54].

Specifically to DRP, multi-mineral segmentation of μ-CT images can be a complex and time-consuming task using traditional segmentation algorithms because the voxel values for different minerals are incompletely differentiated due to similar X-ray attenuation coefficients and Poisson–Gaussian noise [55]. Therefore, most studies treat all minerals as a single solid phase and pores as the other phase [56,57]. However, this is not appropriate in all cases, especially for CCS and UHS. Certain types of minerals will cause hydrogen loss, which is observed in the reaction between H_2-saturated brine and calcite [12]. In addition, CO_2 trapping is characterized by the wettability of different types of minerals [25,58,59]. The utilization of CNN-based multi-mineral segmentation could be one approach to resolve this issue.

For CCS and UHS studies, high pixelwise accuracy does not necessarily guarantee that petrophysical parameters such as permeability or relative permeability are accurately captured. As shown in previous studies, petrophysical parameters are highly sensitive to small segmentation errors [39]. Therefore, the sensitivity of quantitative measurements to these errors must be considered. A segmentation of six mineral phases on a sandstone sample was performed using several CNNs, including SegNet and U-Net [37]; segmentation errors were evaluated in terms of both pixelwise accuracy and physical accuracy. Overall, 95% pixelwise accuracy was achieved, whereas the segmentation results displayed high variance in terms of physical measurements. The commonly occurring phases such as quartz are the main contributors to pixelwise accuracy, while the accuracy of the less commonly occurring mineral phases is lower than the overall accuracy. For example, A study reported that in zircon the phase accuracy was only 60% with an overall pixelwise accuracy of 94% [38]. The issue is that networks tend to overestimate commonly occurring phases and underestimate the less commonly occurring phases when the training data of each phase are imbalanced. This issue was exemplified in the dataset used by [37,38], which contained 61% quartz phase but only 0.21% mica phase as a volume fraction. Less commonly occurring phases are likely recognized as noise by the network and networks; therefore, they train for the commonly occurring phases that dominate the accuracy. It is difficult to balance sparse phases because these minerals are rare in rocks, and obtaining training data in the first place is difficult because of the high expense. Data argumentation of sparsely occurring phases and judicious selection of the loss function during training can be carried out to reduce the imbalance to an extent; for example, focus loss reduces the weight of the easy-to-segment phases and forces the network to focus more on the loss of less common phases [60]. However, because the CNN-based segmentation method is a data-driven task, such imbalances are unavoidable when it comes to less commonly occurring phases.

In addition, μ-CT scanning noise, which is commonly regarded as a random signal and is characterized by a probability density function, is known to significantly influence segmentation results [61,62]. The noise mainly includes Gaussian and Poisson processes [55]. Gaussian noise results from the random distribution of independent signals, whereas Poisson noise is commonly found in situations where photons are accumulated over a detector, such as charge-coupled device (CCD) cameras [63]. The boundary of each mineral phase is difficult to define with Poisson and Gaussian noise because edge detection is highly sensitive to noise, and the image quality is reduced significantly. Therefore, it is common to leverage several noise removal filters before segmentation. These filters mainly include the non-local mean filter and Gaussian filter, which were introduced as edge-preserving denoising and blurring filters to remove additive Gaussian noise [64]. Laplacian, Canny, and Sobel filters are sharpening and edge-detection filters commonly used for boundary detection and feature extraction for supervised machine learning segmentation [65]. However, denoising filters can cause a certain degree of degradation of the details in images and remove the "real information" and fine structures, especially for less-common mineral phases [66]. Although these degraded effects might be acceptable for binary segmentation, they should be strictly avoided in multi-mineral/phase segmentation because these fine structures need to be preserved for segmenting the less-prevalent minerals. For real-time synchrotron-based μ-CT imaging, noise associated with dynamic imaging occurs across all images because the exposure time for each collected radiograph is significantly reduced. Therefore, it is difficult to segment the images. Moreover, CNN-based segmentation is becoming increasingly difficult to perform because of the limited availability of real-time ground-truth datasets due to the time and cost expense. Overall, performing accurate multi-mineral segmentation on real-time data with common Gaussian and Poisson noise is essential for fine structure characterization and dynamic image processing.

The aim of this study is to develop an advanced digital material workflow that is generalizable to various physical problems, particularly imaging systems that have complex micrometer-sized structures composed of multiple phases. Our target system is sandstone rock for CCS and UHS applications, while other applicable systems include but are not limited to fuel cells [67], negative compressibility materials [68], flexible metal-organic frameworks [69] and high-thermal-conductivity porous media [70]. We investigated the potential of unpaired domain transfer between real-time synchrotron-based μ-CT images with associated noise and long-scan traditional μ-CT images to provide a framework for the imaging of dynamic processes. Domain transfer is performed to provide a robust framework because ground-truth segmented data for real-time, synchrotron-based μ-CT images are not always readily available. CycleGAN is widely used for unpaired image-to-image translation [71] and is thus used for transferring synchrotron-based noise to a long-scan μ-CT dataset with a ground-truth counterpart. A total of four CNN architectures were trained to segment the real-time data into six mineral phases. In terms of error assessment, in addition to the commonly used pixelwise accuracy, region-based and physical accuracy are essential metrics. This is because the purpose of segmentation is to facilitate the quantitative assessment of physically meaningful quantities such as interface determination, topological connectivity, and permeability, which are key design parameters for CCS and UHS applications. Overall, this study evaluates a digital material platform for the quantitative assessment of complex porous materials using an unpaired domain transfer mothed for dynamic synchrotron-based μ-CT, providing real-time analysis of physical processes where multiple phases and complex structures are present.

2. Materials and Methods

2.1 Datasets

Unpaired domain transfer was performed between raw μ-CT data and synchrotron-based μ-CT data. A miniplug from the Mt. Simon sandstone reservoir was cored to 5 mm in length and 3 mm in diameter and scanned using μ-CT at the University of New South Wales. The surface of the sample was polished for subsequent mineral classification by quantitative evaluation of minerals using scanning electron microscopy (QEMSCAN). The 2D QEMSCAN mineral maps were then registered to the corresponding cross section of the 3D μ-CT voxel [26]. Following this process, 3D mineral segmentation in the μ-CT image was performed based on the X-ray intensity differences of minerals as guided by the registered 2D QEMSCAN images, which serve as ground truth for the 3D Mt. Simon sandstone μ-CT data. Further details on the data preparation can be found in [37]. In total, the full-size, raw μ-CT data and corresponding GT data were $1100\times1100\times2200$ voxels, as shown in Figure 1 (a) and (b). The GT images are comprised of six phases, labeled from 0 to 5: pore, clay, quartz, feldspar, micas, and a mixed group of less-common high-density minerals.

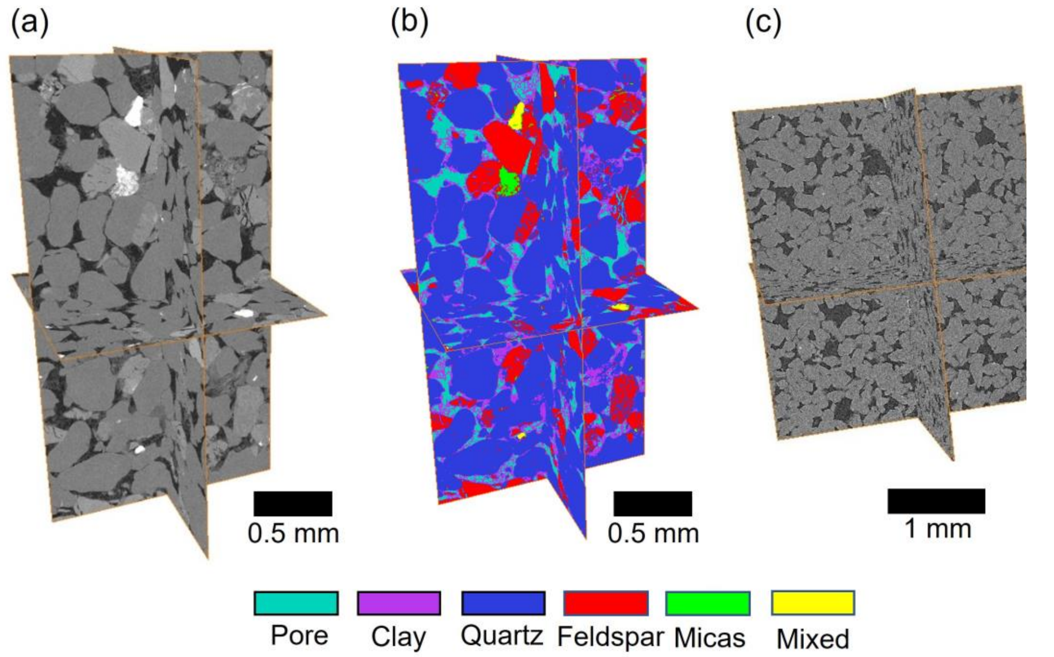

Figure 1: (a) Full-size, raw μ-CT data with a voxel size of 1100×1100×2200. (b) Segmented GT dataset with six phases presented. (c) Full-size, synchrotron-based μ-CT data containing fast-imaging-associated noise, measuring 1000×1000×1200.

Synchrotron-based μ-CT images were obtained from GeoSoilEnviroCARS Sector 13 at the Argonne National Laboratory Advanced Photon Source (APS). Miniplug Bentheimer sandstone was obtained by cutting the rock to 5 mm in diameter and 10 mm in length. The real-time, 3D-synchrotron-based μ-CT scan was then conducted with X-ray photon fluxes of approximately 10^{12}–10^{14} photons s^{-1} during a waterflooding experiment. The 3D images were collected in approximately 20 s at a resolution of 3.5 μm; further details are provided in [32]. It is noted that there is always a tradeoff between sample size and image resolution. While a higher resolution mage may capture fine features of geometry, it will limit the field of view and spatial information at a larger scale that are affecting determination of properties of porous media. For typical flow characterization of sandstone, the resolution is often around 2 to 5 μm [72–74]. The synchrotron-based μ-CT image of the dry Bentheimer sandstone is 1000×1000×1200 voxels in size, as shown in Figure 1 (c). This dataset contains fast-imaging-associated noise that exists across all phases, which makes any attempt at multiphase segmentation challenging. Table 1 gives a summary of the samples and datasets used in this study.

Table 1: Basic information for the samples and datasets used in this study. The nomenclature of each dataset is used throughout this paper.

Samples	Datasets	Nomenclature	Voxel Size
Mt. Simon Sandstone	Long-scan Mt. Simon sandstone μ-CT data	*Raw μ-CT data*	1100×1100×2200
Mt. Simon Sandstone	Domain-transferred Mt. Simon μ-CT data	*Dynamic-based μ-CT data*	1100×1100×2200
Bentheimer sandstone	Synchrotron-based Bentheimer sandstone μ-CT data	*Synchrotron-based μ-CT data*	1000×1000×1200
Bentheimer sandstone	Domain-transferred Bentheimer synchrotron-based μ-CT data	*Static-styled synchrotron data*	1000×1000×1200

2.2 Domain transfer by CycleGAN and image degradation

Noise from the real-time, synchrotron-based μ-CT data was transferred to the raw μ-CT data using CycleGAN. CycleGAN comprises two generators and two discriminators that perform unpaired image-style transfer. The generators were based on an encoder–decoder structure that applies three convolutional layers in the down-sampling steps, followed by nine residual blocks and sequential decoding steps using up-sampling layers instead of transposed convolutional layers to avoid prediction artifacts [75]. Instance normalization was used because of its advantage in image style transfer, which normalizes each image individually without considering the image content of the entire batch [76]. Using this process, the features of the two μ-CT sandstone datasets were captured and transferred between each other by the generators. Two styles of fake μ-CT sandstone images and real μ-CT sandstone images were then processed through two discriminators; PatchGAN [46] was used as a discriminator to determine whether an N×N output was fake or real. Overall, two discriminators were trained to distinguish the fake and real images, while the two generators were trained to produce fake images that appear similar to real images. The detailed workflow of the CycleGAN is shown in Figure 2.

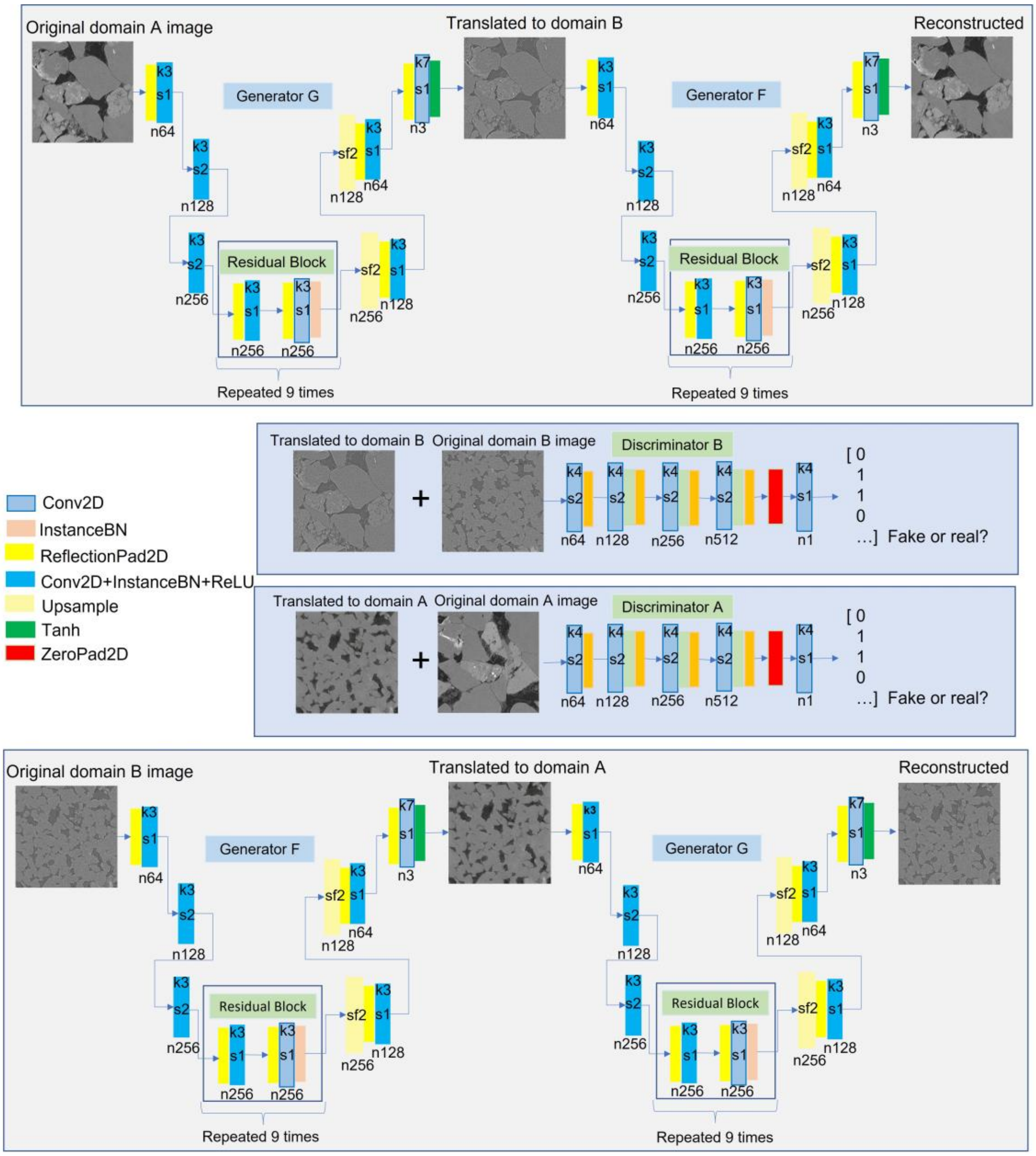

Figure 2: Architecture for CycleGAN. Two generators and two discriminators were used, and the PatchGAN was used as the output for the discriminators. Unpaired domain transfer is performed between raw μ-CT data and synchrotron-based μ-CT data. The letter k refers to the kernel size of the layer, n to the number of channels, s to the stride, and sf to the scale factor for upsampling.

The objective loss function for training the CycleGAN contains two types of loss: (1) adversarial loss and (2) cycle consistency loss. Adversarial loss acts as the loss for the discriminator, whereas the cycle consistency loss acts as the loss for the generator. The total objective loss function is

$$L(G,F,D_X,D_Y) = L_{GAN}(G,D_Y,X,Y) + L_{GAN}(F,D_X,X,Y) + L_{cyc}(G,F) \quad (1)$$

where X, Y are the two different domains. $L_{GAN}(G,D_Y,X,Y)$ includes the loss between the fake image generated by the mapping function G and the real image that needs to be minimized and the loss for the discriminator D_Y to distinguish the fake and real image that needs to be maximized. A similar objective loss, $L_{GAN}(F, D_X, X, Y)$, is used for another mapping function F and discriminator D_X. $L_{cyc}(G, F)$ refers to the losses during feature mapping, including the loss between the real image and the fake image, the fake image with the reconstructed real image, and the real image with the reconstructed real image. The loss function for the adversarial loss is

$$L_{MSE} = \frac{1}{n}\sum_{t=1}^{n}(y - f(x_t))^2 \quad (2)$$

The $L1$ function used for cycle consistency loss is

$$L_{L1} = \frac{1}{n}\sum_{t=1}^{n}|y - f(x_t)| \quad (3)$$

where y is the GT pixel value and $f(x_t)$ is the network prediction. CycleGAN was trained with an initial learning rate of 0.0001 using the Adam solver with a batch size of 8×192×192. In total, the 2D datasets comprised 4800 raw μ-CT images and 4800 synchrotron-based μ-CT images. The data were then split into 4000 images for training and 800 images for testing.

2.3 Image degradation

Gaussian–Poisson noise that commonly exists in μ-CT images results in reduced image quality and subsequently affects segmentation results and further DRP analyses. In addition, the utilization of denoising filters may add additional artifacts and/or smooth finer details of the pore structure. Therefore, by considering the fine structure and topology as highly essential for the segmentation of sparsely occurring minerals, we simulated a scenario where there is a certain degree of Gaussian–Poisson noise in our raw μ-CT data and tested the capability of CNN-based multi-mineral segmentation methods to distinguish minerals with such noise. Gaussian and Poisson noises were manually added to the raw μ-CT data by using a Gaussian filter and Poisson distribution in Numpy and Scipy packages in Python after domain transfer. Random Gaussian noise was added to each image using a Gaussian filter with a standard range of 2–3. Poisson noise was added with the expectation of intervals based on the pixel values of each image. To test whether the degree of noise was realistic, no-reference image quality metrics called BRISQUE and NIQE were calculated using the statistical features of the input image to evaluate the similarity of our data to other dynamic synchrotron-based μ-CT data. Overall, after domain transfer and image degradation, the raw μ-CT data that contained noise associated with dynamic synchrotron scanning and commonly occurring Gaussian–Poisson noise were used to mimic the realistic fast synchrotron-based scanning results. Therefore, instead of attempting to segment directly on the synchrotron-based μ-CT data, the CNN-based network could be trained using the domain-transferred Mt. Simon μ-CT image. This trained network could then be used later to segment a real synchrotron-based μ-CT image.

2.4 Segmentation CNNs architectures and training schedules

Multi-mineral segmentation was performed in 2D using four CNN architectures based on the encoder–decoder structure, which exploits features from the encoding step and recovers the spatial resolution from the decoding step. We decided to train all networks in 2D because the QEMSCAN image was generated in 2D and the domain transfer by CycleGAN was performed in 2D. As shown by [37], networks in 2D and 3D provide similar pixelwise and physical accuracy, while networks in 2D are computationally more efficient compared to 3D because they have fewer trainable parameters. The CNN networks that contain both pre-trained and non-pre-trained models are U-ResNet [37,43], U-ResNet-cGAN [46], U-Net with EfficientNet-B3 as the backbone (EfficientU-Net), and EfficientU-Net-cGAN. The advantages of each network and the main differences are listed in Table 2. The main reasons for selecting these networks are as follows:

(1) U-ResNet has been proven to perform better in multi-mineral segmentation than SegNet and U-Net, which are commonly used for semantic-segmentation CNN networks [37]. Therefore, U-ResNet is tested as a baseline to check whether other networks can perform better.
(2) With the addition of the cGAN module, both binary-cross-entropy loss and cross-entropy loss have been used to regulate training, which is beneficial in preventing overfitting and edge determination.
(3) One of the state-of-the-art network architectures in image classification is EfficientNet, which has the advantage of a high-balancing network depth, width, and resolution. Therefore, we used EfficientNet for feature extraction to improve the training efficiency. In addition, although EfficeintU-Net has more trainable parameters than U-ResNet, the total network size is only 60% of that of U-ResNet.
(4) EfficientU-Net-cGAN, which is combined with the cGAN module, has been proposed to regulate training with high efficiency.

Table 2: A comparison of the tested networks.

Networks	Total parameters	Total network size (MB)	Pre-trained	Loss function	Advantages
U-ResNet	8,761,858	3107	No	Cross Entropy loss	Utilization of long skip connection and short skip connection
U-ResNet-cGAN	19,926,211	3233	No	Cross entropy loss + Binary cross entropy loss	cGAN module is used to further distinguish the output image and binary-cross-entropy loss added to regulate the training

EfficientU-Net	26,063,594	2043	Yes	Cross-entropy loss	Efficient feature extraction by balancing depth, width, and resolution
EfficientU-Net-cGAN	37,225,899	2169	Yes	Cross-entropy loss + binary-cross-entropy loss	Combines the advantages of cGAN module and EfficientNet

A non-pretrained, symmetric U-ResNet with a structure similar to that used by [37] was employed in this study instead of the U-Net with pretrained ResNet as an encoder. The main reason for this choice is that ResNet was originally designed for image classification that contains several repeated residual blocks. However, when it comes to segmentation, a particularly deep and complex encoding process for a symmetric encoder–decoder structure would require a similarly complex decoding process. This means that a large amount of feature information is lost because of the many upsampling layers in the decoding process. Therefore, the U-ResNet used herein requires short-skip connections between each block to preserve shallow image information. Moreover, long-skip connections, which link the encoder blocks to their equivalent decoder blocks and are used in the U-Net, are also used to retain the shallow features of the input image. The U-ResNet architecture is shown in Figure 3.

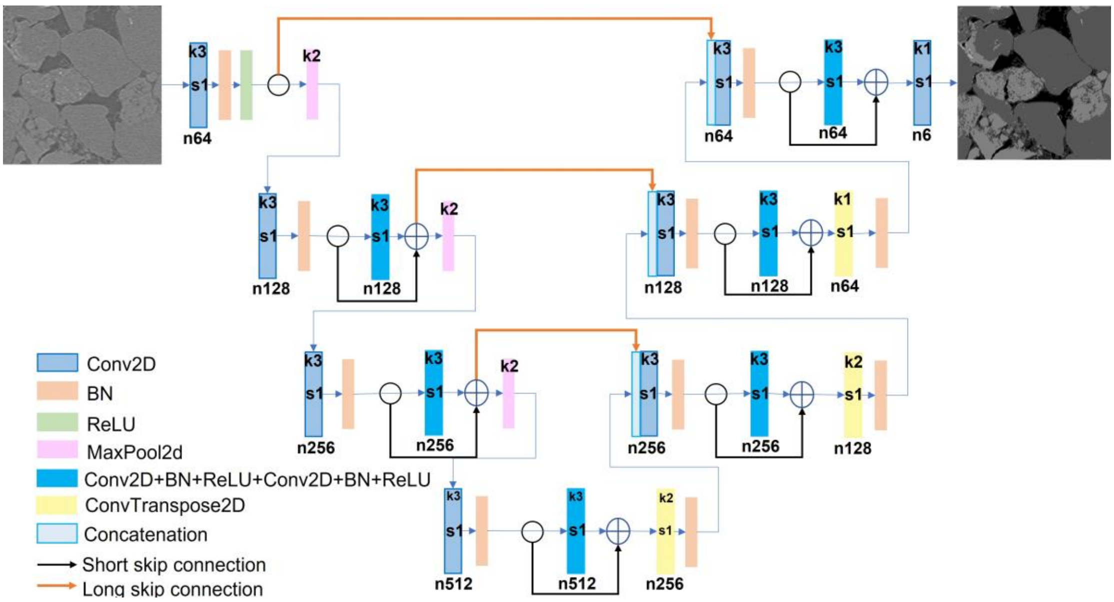

Figure 3: Architecture of the U-ResNet, containing both a short-skip and long-skip connection. The input image contains three channels, and the output has six channels, indicating six different phases.

Based on the U-ResNet structure, an advanced U-ResNet architecture combined with a conditional adversarial network (U-ResNet-cGAN) was introduced. Conditional adversarial networks are designed mainly for image-to-image translation tasks. For the segmentation task, output segmented images are produced after the encoder–decoder structure, and then both the GT and segmented outputs are passed through a discriminator to distinguish whether the image is real or fake. PatchGAN is used here because of its advantage of generating a fixed-size patch instead of a single number after the discriminator. By applying conditional adversarial networks, U-ResNet works as a generator and then competes with the discriminator during training. The detailed architecture of the U-ResNet-cGAN is shown in Figure 4.

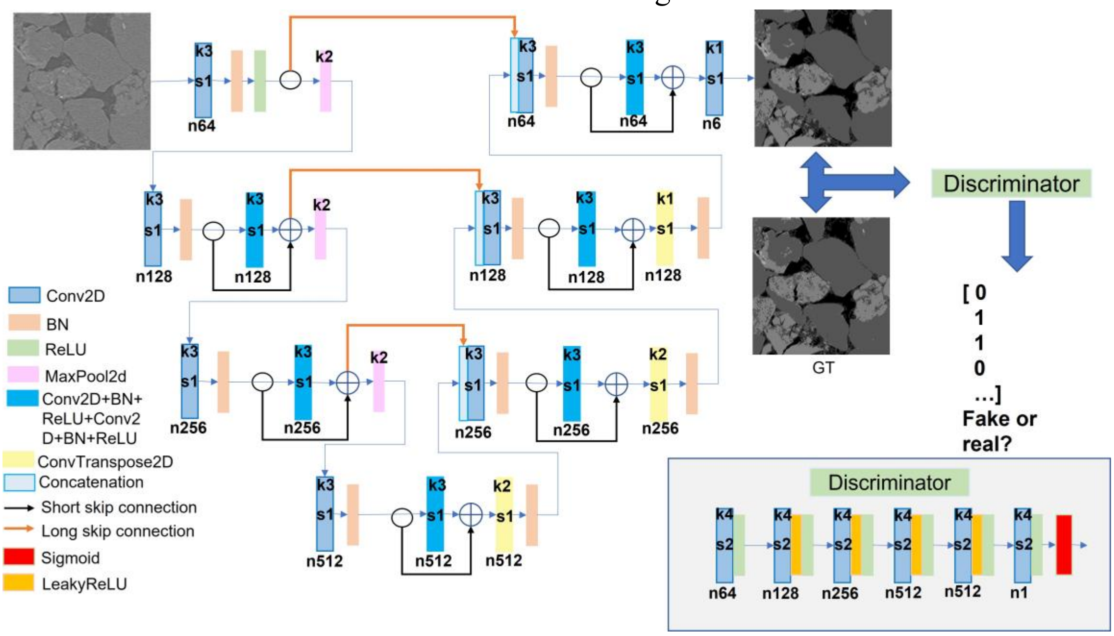

Figure 4: Architecture of the U-ResNet-cGAN. The encoder–decoder structure is similar to the early U-ResNet structure. The output for the U-ResNet with the corresponding GT image is further passed to the discriminator. After application of the Sigmoid function, the output for the patch ranges from 0 to 1.

As discussed previously, for symmetric encoder–decoder structures—particularly for deep, pretrained CNNs that are designed for image classification tasks—are inefficient during the decoding step. However, an encoder–decoder asymmetric structure that contains a deep, complex network structure in the encoding step and a simple network structure in the decoding step could solve this issue and further improve feature extraction and identification. Therefore, in this study, EfficientNet-B3 [44] which achieves high accuracy and efficiency in image-classification tasks, was used as a feature extractor in the encoding step. Several transposed, convolutional layers were used directly to increase the feature shape to the same size as the input image to avoid feature loss. Several long-skip connections were used to retain the shallow features of the input image. The network architecture of the EfficientU-Net-B3 is shown in Figure 5. The core structure contained 25 blocks that use a structure similar to MobileNet [77]. The overall design concept was based on the utilization of inverted residual structures and residual blocks. A 1×1 convolution was used before the 3×3 or 5×5 network structure to increase the dimension, and an attention mechanism that assigns a weight to each feature of the image was added after the 3×3 or 5×5 network structure.

An advanced EfficientU-Net was then proposed by introducing a conditional adversarial network called EfficientU-Net-cGAN, and its architecture is shown in Figure 6. The discriminator that distinguishes the output segmented image from the GT had a similar structure to that of the U-ResNet-cGAN, as shown in Figure 4.

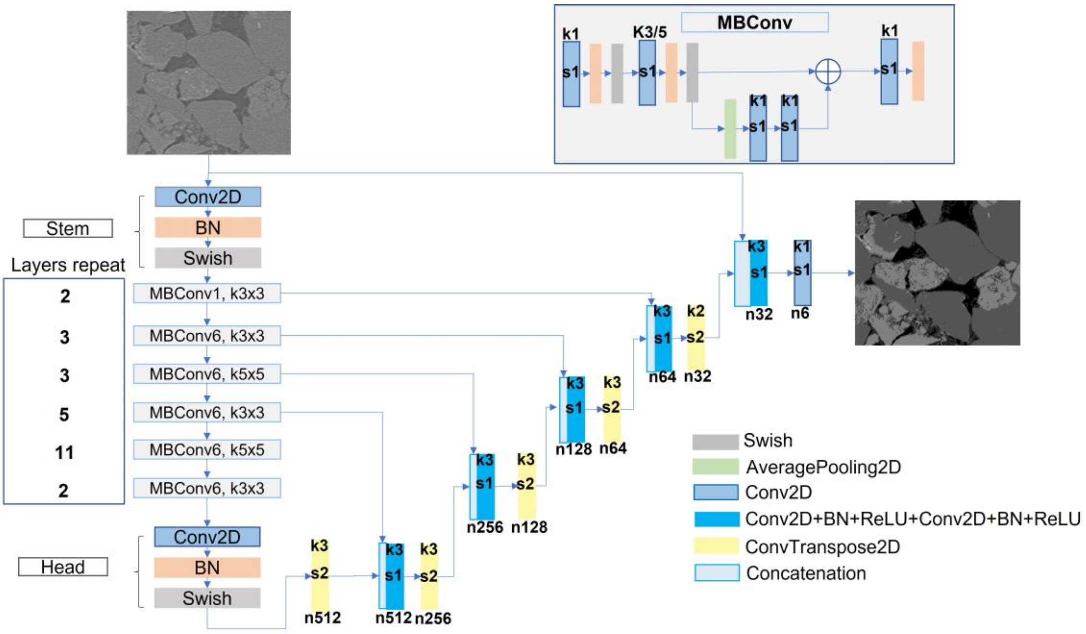

Figure 5: Architecture of the EfficientU-Net-B3. The encoder contains a Stem layer, 25 MBConv blocks, and Head layer. The decoder contains five upsampling layers with long-skip connections between encoding layers.

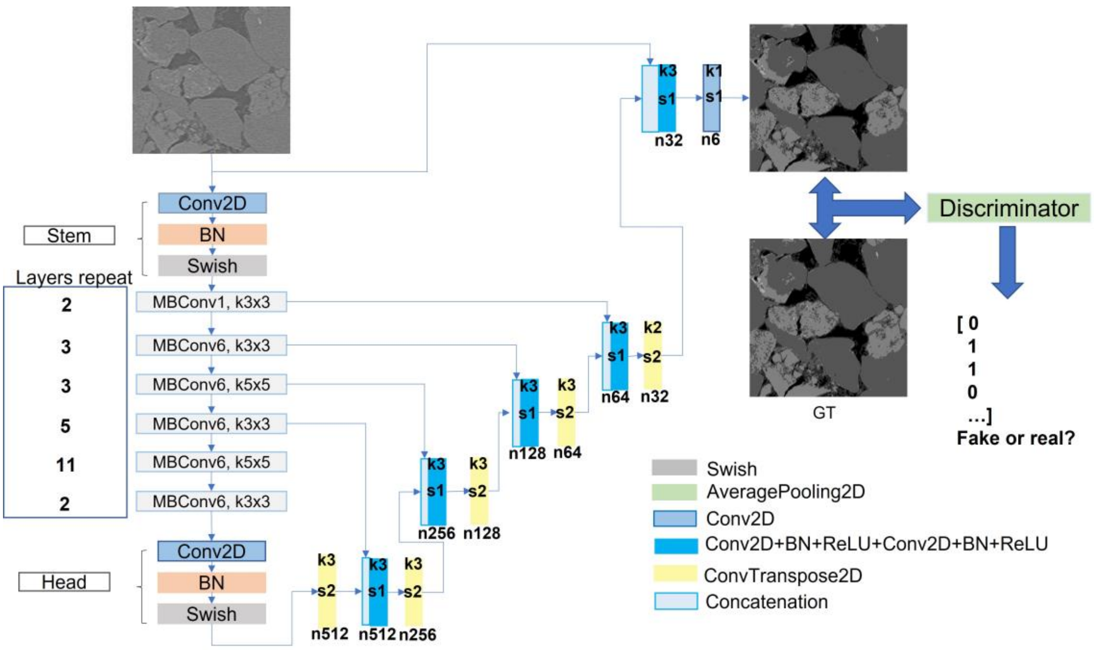

Figure 6: Architecture of EfficientU-Net-cGAN. The encoder–decoder structure is identical to the previous EfficientU-Net-B3 structure. The addition of a discriminator would further force the output segmented image to appear similar to GT. The discriminator structure is identical to the discriminator depicted in Figure 4.

All networks were trained for 40 epochs with an initial learning rate of 0.0001 using the Adam solver. The input images were cropped to 454×454 with a batch size of five. The learning rate is reduced by a factor of 0.5 when the loss reaches a plateau for eight epochs. The loss function used to train all networks is the cross-entropy loss:

$$cross\ \ entropy\ \ =\ \ -\sum_{k=1}^{N}(p_k log q_k) \tag{4}$$

where p is the GT target in scalar, and q is the prediction after the softmax function. For the U-ResNet-cGAN and EfficientU-Net-cGAN, an extra binary cross-entropy loss is applied to regulate the training of the discriminator:

$$binary\ \ cross\ \ entropy = \ -\sum_{k=1}^{N} w_k[p log q_k + (1-p) log(1-q_k) \tag{5}$$

The training dataset contained 8,800 degraded μ-CT images split into 7,200 for training and 1,600 for testing. The training was implemented on PyTorch, using an Nvidia RTX 3090 graphics-processing unit.

2.5 Physical Accuracy Measurements

Aside from pixelwise accuracy, physical accuracy was also important to measure because in DRP the objective of segmentation is to isolate each mineral phase for subsequent physical analyses. In this study, physical accuracy was first evaluated by connectivity and porosity. Other non-trivial physical parameters that reveal the behavior of fluid displacement in rock are absolute permeability and relative permeability. Absolution permeability is sensitive to porous structure, while relative permeability is sensitive to both porous structure and mineral occurrence that are determined by multi-phase segmentation [78]. These parameters are calculated based on a mixed-wetting condition that commonly occurs in reservoir rock and can be qualified by comparing the network output with the GT [79,58,80]. The Euler characteristic (χ) is used as an indication for connectivity, which is calculated as the difference between the number of loops and the number of disconnected pixels. The equation for calculating χ is

$$\chi = objects\ -\ loops\ +\ holes \tag{6}$$

In addition, the volume fraction was determined for all phases, which was calculated by dividing the phase volume by the total volume; the pore-phase volume fraction is the porosity of the sample. The absolute permeability was calculated using an MRT-LBM (multirelaxation time lattice Boltzmann method) preconditioned with a domain-decomposed Laplace solver [81–83], and the relative permeability was solved using the MorphLBM method [27].

MorphLBM utilizes a multiphase LBM simulation routine directly in the pore space of the image and performs morphological updates on the phases to emulate steady-state fluid configurations in an accelerated manner compared to directly simulating the co-injection of fluids, which requires significant simulation time to move through the domain. Fluid configurations are updated with small increments of erosion or dilation (depending on drainage or imbibition) to target saturation. LBM simulation was performed continuously as these small morphological increments were performed, and when the target saturation was reached, the LBM simulation was run until the capillary number converged. When the capillary number converges, the steady-state relative permeability point is recorded, and the morphological updates are started again. In this study, morphological imbibition was performed on the domains initialized by simulated primary drainage to residual saturation. The morphological updates were performed at a distance of 0.1 by interpolating the phase indicator value, and relaxation was performed for 1000 LBM timesteps between morphs. The saturation increments were 5%, and the capillary number tolerance was set to less than 1×10^{-3} per 1000 time steps of the 50,000 timestep exponential moving average, and the relative variance was less than 0.01. The system capillary number was maintained at 1×10^{-5} to emulate capillary-dominated two-phase flow. Mixed wettability was easily modeled using the LBM method (Color LBM) by simply assigning the contact angle as an affinity between –1 (water) and +1 (oil) for various solid voxels, where the static contact angle is equivalent to the inverse cosine of the affinity [84].

3 Results and Discussion

3.4 Image degradation results

The raw μ-CT data was degraded by transferring fast-imaging-associated noise from the synchrotron-based μ-CT data, followed by the addition of Gaussian–Poisson noise. This unpaired domain transfer was performed using CycleGAN. A sample output from CycleGAN is provided in Figure 7, which includes the dynamic-styled μ-CT data and static-styled synchrotron data. Because this study mainly focuses on the segmentation of degraded images, only the domain transfer from raw μ-CT data to dynamic-styled μ-CT data was required. Furthermore, the output dynamic-styled μ-CT data was further degraded by adding Gaussian–Poisson noise, as shown in Figure 7 (e). Figure 7 (f) shows an example of a GT image. To determine whether the degree of noise added was realistic, two image-quality metrics were calculated using predictable statistical features to compute a quality score: the blind/referenceless image spatial quality evaluator (BRISQUE) and the naturalness image quality evaluator (NIQE), which provide a qualitative measure of noise. These two methods do not require a paired reference image for image quality measurement, as required for the presented data, because domain transfer is performed between unpaired images. A detailed theoretical background of BRISQUE and NIQE can be found in [85,86]. The BRISQUE and NIQE metrics were compared between the raw μ-CT data, synchrotron-based μ-CT data, and degraded dynamic-styled μ-CT data, as well as two other existing dynamic-synchrotron-based μ-CT images that are accessible on the Digital Rock Portal (https://www.digitalrocksportal.org). The first dataset is the synchrotron-based μ-CT image of Ketton limestone [87] and the second is the synchrotron-based μ-CT image of Gildehauser Sandstone [88]. The results of the BRISQUE and NIQE metrics for each dataset are listed in Table 3. For both metrics, a lower score reflects better image quality. As shown in Table 3, the raw μ-CT data had the best image quality, while the other dynamic datasets were of lower quality. For the degraded dynamic-styled μ-CT data, both metrics demonstrated that the image quality after domain transfer and degradation was within a reasonable range of commonly used dynamic synchrotron-based μ-CT data.

Table 3: Image-quality measurement of five datasets. Both BRISQUE and NIQE were calculated slice by slice, and the average value of all slices was taken. The final degraded dynamic-styled μ-CT data had a similar image quality as the other three synchrotron-based μ-CT datasets.

	BRISQUE	NIQE
Raw μ-CT data	17.9	3.4
Synchrotron-based μ-CT data	42.3	11.0
Degraded dynamic-styled μ-CT data	43.4	8.9
Synchrotron-based Gildehauser Sandstone μ-CT data	30.5	6.8
Synchrotron-based Ketton limestone μ-CT data	40.8	6.2

Comparing the red regions in Figure 7 (c) and (e), it can be seen that the pixel value difference between feldspar and quartz is reduced after degradation, which could result in errors during segmentation. To evaluate the performance of CycleGAN, the voxel distribution of the 3D volume ($500\times500\times1200$) of raw μ-CT data, synchrotron-based μ-CT data, and dynamic-styled μ-CT data were compared, as shown in Figure 8. The variances of the normalized images that show the difference in voxel distribution were then measured to validate the performance of the domain transfer. It should be noted that because both Mt. Simon sandstone and Bentheimer sandstone consist of a significant amount of quartz, the pixel distribution peaks (indicating the quartz phase) for the raw μ-CT data and synchrotron-based μ-CT data are at the same location. In addition, the results demonstrate that the raw μ-CT data and synchrotron-based μ-CT data have different pixel distributions in a range lower than the pixel value of 100 and at the location where the pixel value is 255 (with a variance of 0.015). After applying domain transfer, the pixel value of the dynamic-styled μ-CT data was consistent with the synchrotron-based μ-CT data, with a variance of 0.002, indicating that CycleGAN is sufficient for the domain transfer of synchrotron noise. The degraded dynamic-styled μ-CT data were subsequently used in the next step of multi-mineral segmentation.

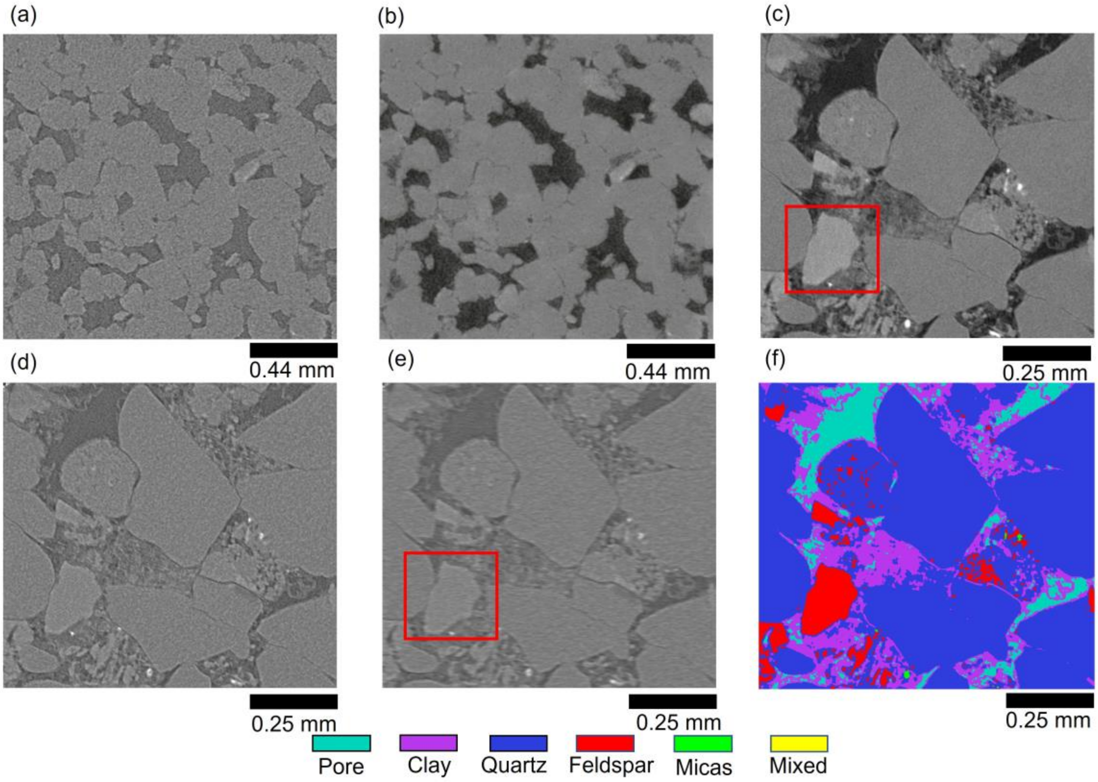

Figure 7: (a) Sample image transferring from synchrotron-based μ-CT data to the (b) static-styled synchrotron data, and (c) raw μ-CT data to the (d) dynamic-styled μ-CT data. (e) Further degradation of dynamic-styled μ-CT data by the addition of Gaussian–Poisson noise. (f) Ground truth QENSCAN slice of the corresponding μ-CT slice.

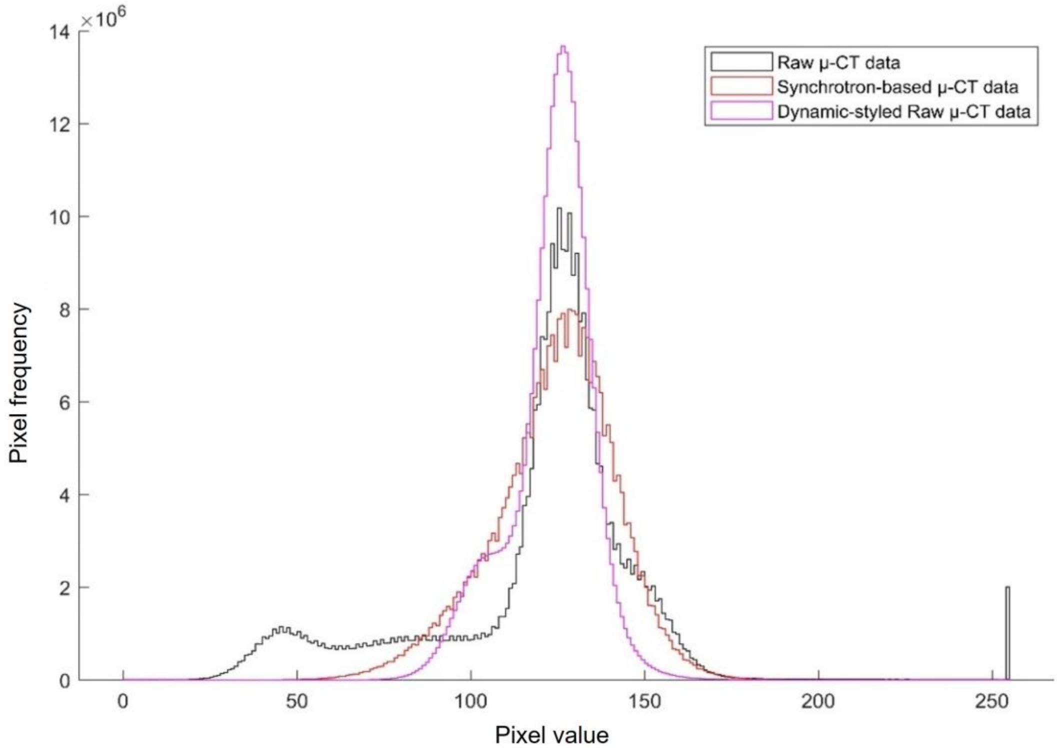

Figure 8: Pixel value comparison between long-scan μ-CT images, synchrotron images, and

the domain-transferred, dynamic-styled Mt. Simon images before adding Gaussian–Poisson noise.

3.5 Multi-mineral Segmentation Accuracy

All networks were trained on data containing dynamic-styled μ-CT data that were cropped into a domain of 454×454×7200 voxels and test images of 454×454×1600 voxels. The weighted accuracy, which considers the correctly labeled pixels as well as the volume fraction of each mineral, was utilized to evaluate each network. Phase accuracies were also calculated to evaluate the ability of the networks when dealing with different minerals. This was performed by averaging the phase accuracies of the last 10 epochs, where the testing accuracy curve of each network reached a plateau. The testing accuracies are shown in Figure 9, with the visualization of a region of interest in Figure 11. The accuracy of all networks converged to approximately 0.94. The accuracy for EfficientU-Net and EfficientU-Net-cGAN was marginally better than that of U-ResNet and U-ResNet-cGAN, with a difference of approximately 0.1% in pixelwise accuracy. Compared to the weighted accuracy used by [37], which included the μ-CT image as input, the accuracy was reduced by 3% as a result of degradation. Overall, all networks performed well, even with synchrotron and Gaussian–Poisson noises, which is also supported by the data given in Figure 10. In this figure, all segmented outputs are visually similar to the GT slice, even for sparse minerals. For example, in the black box presented in Figure 10, the clay and feldspar are sparsely distributed across the quartz; these sparse clay and feldspar phases are easily distinguishable as noise because the input synchrotron-styled Mt. Simon images already contain several types of noise across the entire pore region. However, the networks could correctly label these two minerals in the pore space (black region). Some errors occur in the feldspar (black region) due to the reduction of the pixel value difference between quartz and feldspar, as discussed further in Section 3.1.

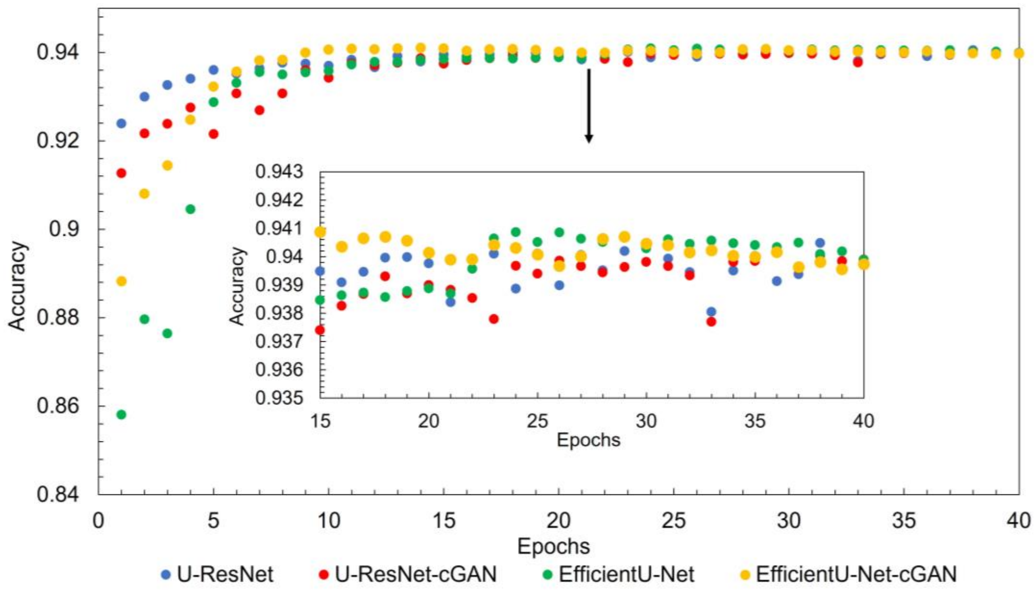

Figure 9: Testing accuracy for four networks. The accuracy for all networks converged to

around 0.94 after 15 epochs. An amplified curve shows that EfficientU-Net and EfficientU-Net-cGAN slightly outperformed the other two networks.

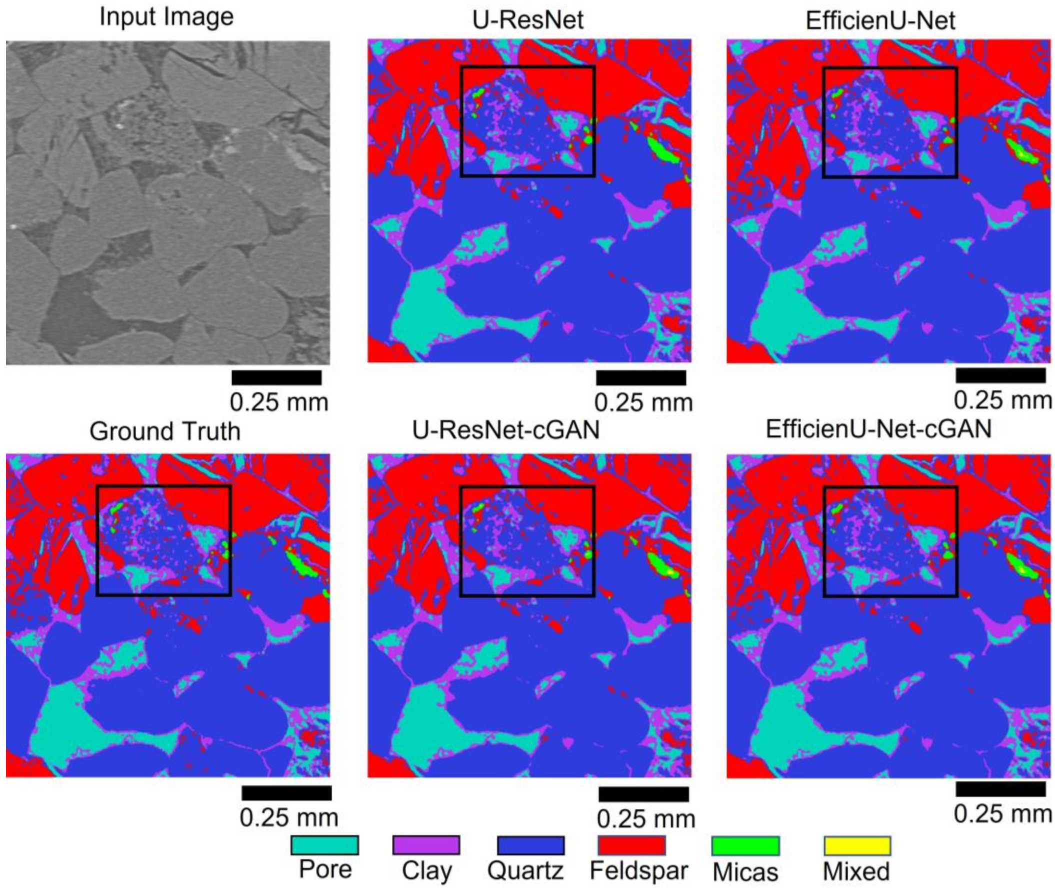

Figure 10: A slice of the testing dataset and output of four networks. All networks visually performed well; however, in the black section, all networks failed to capture the fine bodies of feldspar and clay that exist in quartz.

Because all networks performed similarly in terms of total accuracy, it was necessary to investigate how they performed for each mineral phase; therefore, the phase accuracy was calculated during each epoch. The average phase accuracy was obtained by averaging the phase accuracy of the last 10 epochs, as listed in Table 4. U-ResNet and U-ResNet-cGAN architectures achieved a higher pore-phase accuracy than the two EfficientNet-based architectures, whereas EfficientU-Net and EfficientU-Net-cGAN could better identify the clay phase. All networks performed best in the quartz phase, with an accuracy higher than 0.96, because all networks tended to learn well with a commonly occurring phase. EfficientU-Net-cGAN showed marginally higher accuracy in the feldspar and mica phases. In sparsely occurring micas and mixed-mineral phases, all networks resulted in low accuracy, with approximately 0.7 in micas and 0.5 in the mixed-mineral phase, which further indicated that the volume fraction of each phase is an essential factor that influences the CNN segmentation. Owing to the low phase-volume fraction, the quantity of phase labels was imbalanced, and the networks tended to learn more from the commonly occurring phases, sacrificing accuracy in sparsely occurring phases. In general, all networks could achieve an accuracy in the 85–97%

range for the four most-common phases, indicating that even for the μ-CT image with synchrotron-based noise and for a certain degree of degradation, CNN networks arguably provided accurate pixelwise results for multi-mineral segmentation.

Table 4: Average phase accuracy for identified minerals using four networks as well as the volume fraction of each phase. Overall, each network has its strength in different mineral phases.

	Vol (%)	U-ResNet	U-ResNet-cGAN	EfficientU-Net	EfficientU-Net-cGAN
Pore	7.941	0.924	0.926	0.898	0.905
Clay	11.781	0.855	0.852	0.869	0.860
Quartz	63.185	0.963	0.966	0.965	0.963
Feldspar	16.460	0.901	0.891	0.895	0.904
Micas	0.293	0.694	0.708	0.675	0.713
Mixed	0.339	0.540	0.476	0.536	0.502

Furthermore, the Euclidean distance of the wrongly labeled pixels and the region-based error from an interface were calculated for each 530×530×1600 voxel dataset. This approach was used because the interface between phases is considered to be the most complicated region to segment [89]. It is not directly evaluated by pixelwise accuracy because the majority of the pixels are internal to a given phase and are thus easy to segment. Considering that the objective of segmentation for DRP is to perform further physical analyses, the interface-region-based accuracy and the influence of segmentation on sequential pore characterization and pore-scale simulation should be thoroughly evaluated to show how well each network segments difficult regions, thus revealing the "true" phase structure [90,91]. Therefore, the data were prepared according to the following steps:

1. Each phase's wrongly labeled pixel distribution was first determined by subtracting each network's output from the GT. Meanwhile, the Euclidean distance maps for each phase based on the GT images were generated.
2. The incorrectly labeled pixel distribution was multiplied with the Euclidean distance map for the respective phase, which provides the Euclidean distance of the wrongly labeled pixels from the interface of the given phase.
3. A histogram of the Euclidean distances for the GT data was generated to provide the total number of pixels that are located at a given distance from the interface.
4. The region-based error was calculated by dividing the number of incorrectly labeled pixels that are located at a given distance by the total number of pixels in the GT that correspond to the given distance.

In Figure 11, wrongly labeled pixels in all six phases mainly arise from the Euclidean distance within 1 pixel, indicating that most of the error for all networks is derived from the interface determination. EfficientU-Net-cGAN shows the lowest error near an interface in terms of pore and feldspar phases, indicating that EfficientU-Net-cGAN provides better segmentation at the boundary of these phases. Moreover, U-ResNet provides a better interface segmentation in the clay and mixed phases, whereas U-

ResNet-cGAN can handle the interface segmentation of the quartz and mica phases. It is noteworthy that not all networks can provide an accurate segmentation of the mixed phase near the interface, with the lowest region-based error being only 62%. This is mainly because the mixed phase has an extremely high pixel value in the grayscale image in the raw μ-CT data, but in the synchrotron-based μ-CT data, it does not contain high-density mineral components. Therefore, after domain transfer, in the dynamic-styled μ-CT data, the grayscale value between the mixed phase and other phases decreased, making the segmentation of the mixed phase more difficult.

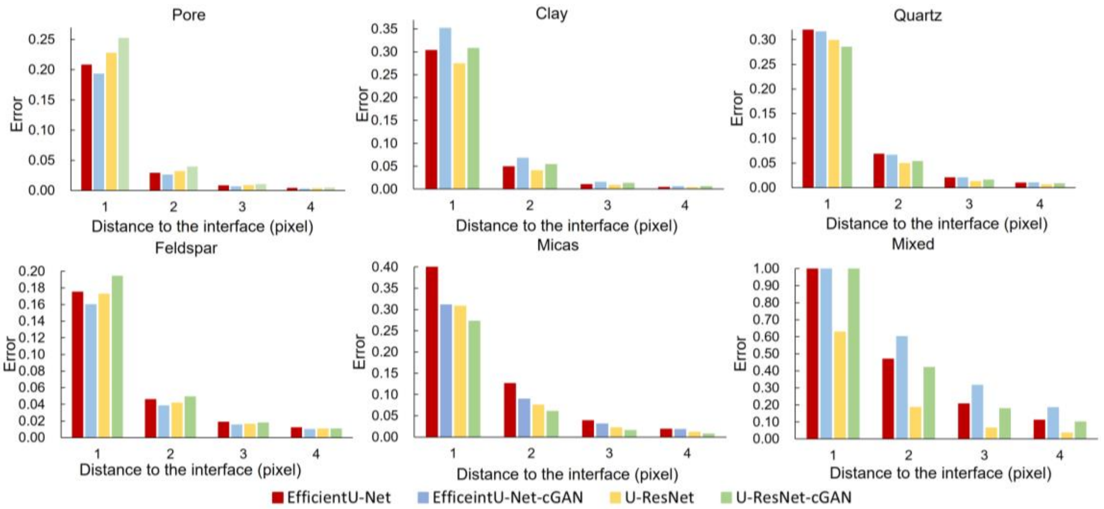

Figure 11: Histograms of the region-based segmentation error of the wrongly labeled pixels in the interfaces of six phases for four networks. The main segmentation error arises from the pixels closed to the phase interface.

3.6 Physical accuracy measurement

In addition to the pixelwise accuracy of each network, the physical accuracy of the segmented outputs is critical for the DRP. Connectivity, volume fraction, absolute permeability, and relative permeability were the physical parameters considered for a mixed-wet condition. The physical accuracy was measured in the domain of $530\times530\times1600$ voxels. First, the volume fraction of each phase was calculated, as shown in Figure 12. It can be observed that U-ResNet-cGAN performed best in the volume fraction of the pore phase, with a difference of less than 0.1% (i.e., porosity), whereas EfficientU-Net yielded an accurate prediction for the quartz and feldspar phases, with differences of 0.2% and 0.3%, respectively. Moreover, U-ResNet performed best in clay, micas, and mixed phases, with differences of 0.4%, 0.6%, and 0.9%, respectively.

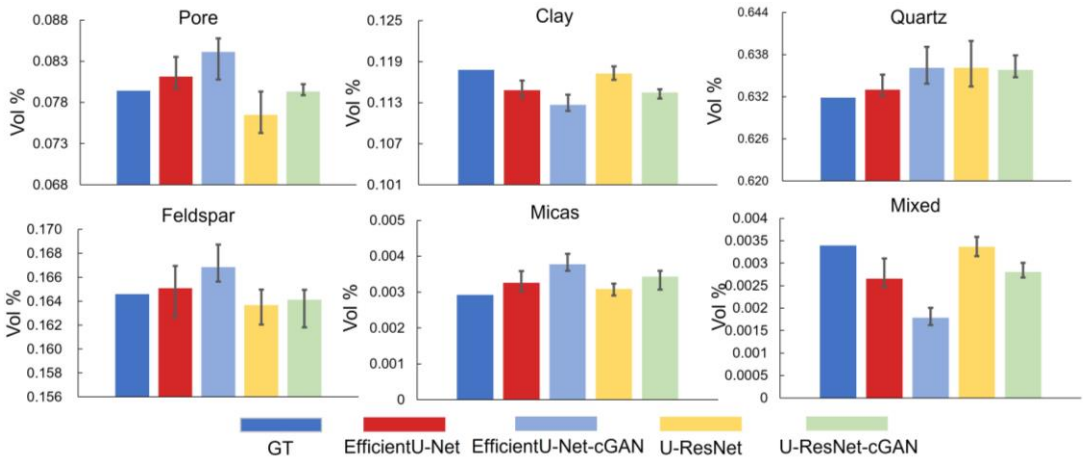

Figure 12: Bar charts showing the volume fraction of each phase compared to the ground-truth result for four networks. Porosity is described by the pore volume fraction. Error bars represent the range of volume fraction calculated based on the top-five most accurately trained epochs of each network.

The connectivity, as described by the Euler number (χ) of each phase, was determined from the segmented images, where χ is a topological invariant defined by the number of objects, loops, and holes in a given phase [92]. The χ values for each phase are presented in Figure 13. In terms of connectivity, it was found that none of the segmented datasets compare well with the GT data. In addition, the variability of the results across all networks was relatively high. The percent differences of χ measured by each network in relation to the GT result are listed in Table 5. Interface pixel errors and existing disconnected small bodies are likely the main reasons for the variations in χ.

Specifically with respect to χ, as shown in Eq. 6, a more positive value for a phase means that there are more isolated objects or fewer loops, indicating that the phase is less connected. On the other hand, a more negative value means that there are more loops than isolated objects, indicating that the phase is well connected. Therefore, it can be seen in Figure 13 that in the pore phase, the χ value for GT is more negative than for any other network result. This suggests that all networks provided segmented images that were less connected than the GT. EfficientU-Net-cGAN provides the most accurate result in terms of the pore phase, being only 6% less negative compared to the GT. For Mt. Simon sandstone, clay fills the pore space, and the less-connected pore phase results in a more-connected clay phase. Therefore, all networks yielded a more negative value of χ in the clay phase. U-ResNet performed best in the clay phase, with only a 1% difference compared to the GT, while the other three networks produced a larger difference compared to GT in the range of 17– 38%. The most accurate result for all networks was found for the χ of the quartz phase. It might be concluded that because quartz is the most abundant phase, the networks tended to train for it more often compared to the other phases, resulting in the highest physical accuracy in terms of connectivity. Moreover, U-ResNet-cGAN provides the best result in the feldspar phase, but the difference was still ≈33% compared to GT, while all other networks provided a significantly negative value of χ compared to GT. In addition, in the mixed-mineral phase, the χ of U-ResNet showed a mere 10% difference compared to GT, while other networks yielded a difference greater than 30%. In addition, all networks underestimated χ in the mica phase, with a difference greater than 50%. This is because the mica phase is rare and mainly consists of many small bodies; in many cases, the networks misidentify these small bodies, which results in fewer isolated objects.

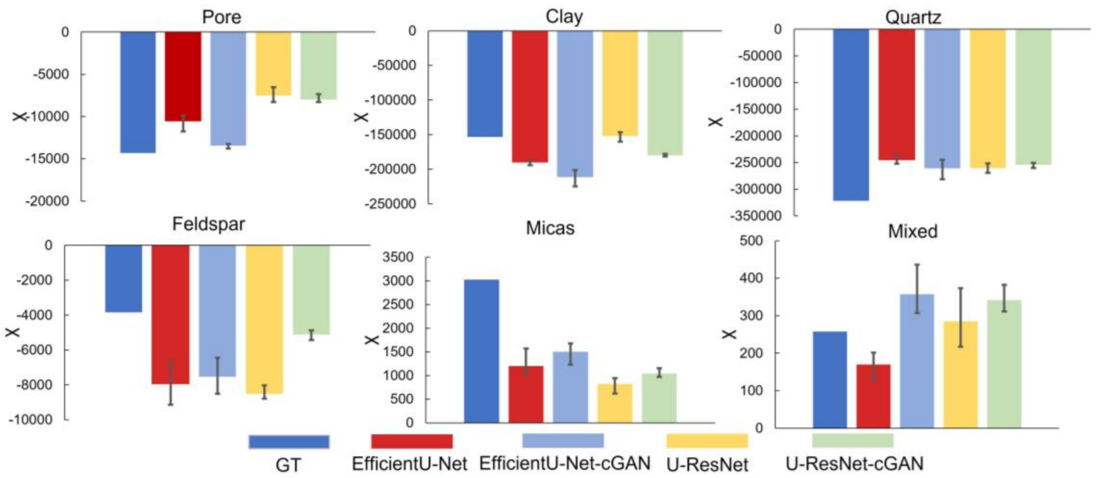

Figure 13: Bar charts depicting the Euler Characterization of each phase compared with the ground-truth result for four networks. The value of χ was calculated by averaging the χ of the network outputs with the top-five pixelwise accuracy. The error bars represent the range of χ calculated based on the top-five most accurately trained epochs of each network.

Table 5: Differences of χ measured by each network compared with GT.

	EfficientU-Net	EfficientU-Net-cGAN	U-ResNet	U-ResNet-cGAN
Pore	27%	6%	48%	45%
Clay	24%	38%	1%	17%
Quartz	24%	20%	19%	21%
Feldspar	107%	96%	122%	33%
Micas	60%	50%	73%	65%
Mixed	34%	39%	11%	32%

The flow characteristics of segmented images are an essential measure of the physical accuracy. The absolute permeability of the pore phase was determined using single-phase flow simulation. After simulating the whole volume, it was further cropped into 24 subblocks with a domain size of 256^3 voxels. The absolute permeability was then calculated for each block, and the results are shown in Fig. 14. A close match was achieved by the EfficienU-Net-cGAN output in terms of the absolute permeability of the bulk volume, as shown in Figure 14 (a). A possible reason for this is that the EfficienU-Net-cGAN provides the closest match in terms of χ in the pore phase; the absolute permeability is known to be sensitive to the pore-phase connectivity [93]. To further test the absolute permeability, 24 subblocks were generated and simulated, as shown in Figure 14 (b). The mean square error (MSE) is reported in Table 6, using these subblocks for each network. It is noted that the absolute permeability could not be calculated in the case where the subblock is formed without a pore phase. All networks provided accurate absolute permeabilities in the majority of the subblocks, with

EfficientU-Net-cGAN providing a marginally lower MSE value; this further confirmed that the connectivity of these blocks is an essential parameter that affects the bulk absolute permeability. The accurate EfficienU-Net-cGAN result for the bulk absolute permeability is highly related to the matched pore-phase connectivity.

Table 6: MSE results for the absolute permeability of these subblocks for each network. EfficientU-Net-cGAN gives a marginally lower MSE, which is consistent with the whole block absolute permeability result.

	U-ResNet	U-ResNet-cGAN	EfficientU-Net	EfficientU-Net-cGAN
MSE	0.1459	0.1460	0.1475	0.1453

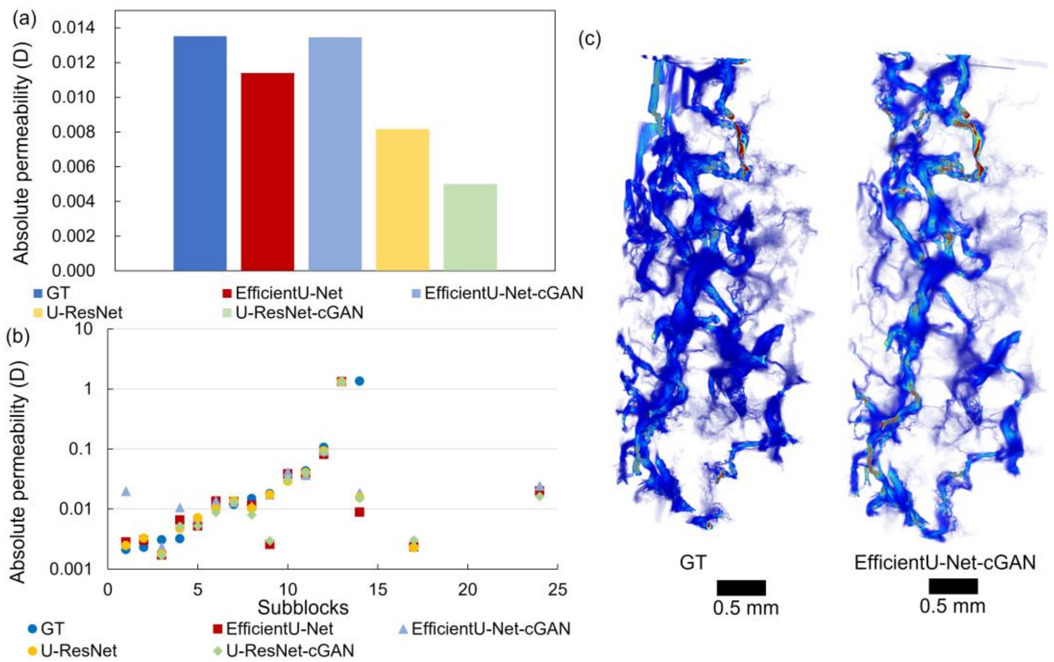

Figure 14: (a) Absolute permeability comparison of each network's output domain, with the closest match achieved by EfficientU-Net-cGAN; EfficientU-Net yielded the second-most-accurate prediction. (b) Absolute permeability comparison of subblocks. All networks showed an accurate estimation in the subblocks. (c) Visualization of the velocity field of the GT and the best-matched network output, as obtained from MRT-LBM on a 530×530×1600 voxel domain. The velocity field images are visually similar, but at some locations EfficientU-Net-cGAN resulted in a higher velocity due to the narrow flow path.

The same domain used for the absolute permeability simulation was used for the relative permeability simulation based on a mixed-wetting condition. The wettability of the quartz phase varies from water wet (contact angle typically ranging from 0°–55°) to intermediate oil water (contact angle typically ranging from 100–140°) [94]. In the Mt. Simon sandstone sample, feldspar exists with quartz to form the grain, and the wettability of both the quartz and feldspar phases in the simulation was assigned as intermediate water wet, with contact angles of 45° and 60°, respectively [58]. For the clay phase, the wettability ranges from intermediate water wet to intermediate oil wet, which depends on the composition (e.g., kaolinite, illite, and montmorillonite) of the clay minerals [58,95,96]. In this simulation, we assigned the clay phase as oil-wet with a contact angle of 120° to provide a mixed-wetting condition. Micas and mixed phases were sparsely occurring phases, so they were set to have a contact angle of 0°. The relative permeability results for all datasets are shown in Figure 15.

The morphLBM method [27] first performs morphological initialization of primary drainage using a local distance maximum transform with hydraulic connectivity considered. Then, multiphase LBM simulations are performed until the system reaches a steady-state configuration for the given saturation. This is determined by tracking the system capillary number and identifying when the relative exponential moving average of relative permeability diverges by less than 1×10^{-3}, and the relative variance is less than 0.01. Once this point is reached, the relative permeability values for the given saturation are recorded, and a negative morphological shell aggregation operation is performed until the fluid saturations reach a desired incremental change, that is, 5% saturation. Once this saturation is reached by morphological shell aggregation, LBM relaxes phase distributions and redistributes the phases among the pore space until a steady state is reestablished, as defined previously. An in-depth description of this method is available in [80]. The shape of the relative permeability of the GT domain simulated using mixed wetting conditions resembles the curves obtained in a similar study of relative permeability in mixed-wetting Mt. Simon sandstones [58]. However, for the U-ResNet-cGAN output domain, the simulation did not converge because of the existence of an extremely narrow flow path. The extremely low absolute permeability of U-ResNet-cGAN is also due to the same reason. Therefore, only the relative permeability curves based on the output domains of the other three networks were reported.

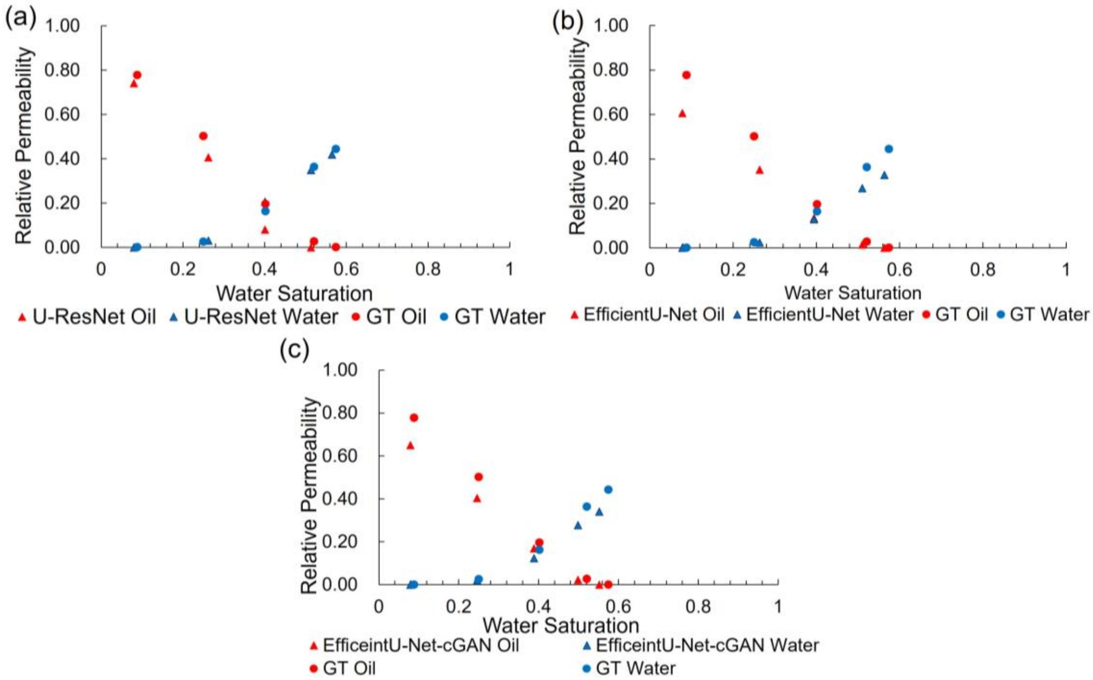

Figure 15: Relative permeability curves for (a) U-ResNet output with GT, (b) EfficeintU-Net

output with GT, and (c) EfficeintU-Net-cGAN with GT, which have a similar shape. The U-ResNet output gives the best match for the endpoint oil and water relative permeability relative to GT, while EfficientU-Net gives the closest crosspoint value and irreducible oil saturation to GT.

The simulation begins with a water saturation of 0.1 and oil saturation of 0.9, ending when the two phases are hydraulically disconnected. The shape of the relative permeability curves for all simulation domains was similar to that of the GT domain. To further analyze the accuracy of the relative permeability, endpoint relative permeability, irreducible saturation, and crosspoint values were compared for each network's output with the GT results, as shown in Table 7. These are particularly important parameters for CCS and UHS applications with irreducible saturations, defining how much of a given phase is trapped in the rock and the crosspoint defining how saturation waves propagate through a reservoir [97]. The endpoint relative permeability for the GT domain is 0.44 for water and 0.78 for oil. The best-performing network is U-ResNet, where the relative permeability value is 0.35 for the water endpoint and 0.74 for the oil endpoint. In addition, the crosspoint relative permeability value for GT is approximately 0.4; the best performance was achieved by the domain of EfficientU-Net, with a crosspoint value of 0.39. The most-accurate result in terms of irreducible oil saturation was also produced by EfficientU-Net, with a value of 0.56 compared to 0.57 for the GT domain. It is worth noting that small clay features that are easily washed-out during segmentation play a significant role in the relative permeability; therefore, this further stresses the importance of preserving fine regions such as fine clay structures and mineral interfaces during segmentation. Figure 16 visualizes the fluid-phase distributions, which shows the fluid distributions at high and low oil saturations. The fluid distributions differ for each segmentation domain, which means that the fluid flow and displacement in the porous media is directly influenced by the multi-mineral phase segmentation. Overall, EfficientU-Net and U-ResNet are visually more like the GT than EfficientU-Net-cGAN.

Table 7: Comparison of endpoint relative permeability value, irreducible oil saturation, and crosspoint values between each network with the GT. The parameter k_{rwr} refers to water endpoint relative permeability, k_{ror} to oil endpoint relative permeability, s_{wcp} to the water saturation at the crosspoint, and s_{or} to irreducible oil saturation.

	GT	UResNet	EfficientNet	EfficientNetGAN
k_{rwr}	0.44	0.35	0.33	0.34
k_{ror}	0.78	0.74	0.61	0.65
S_{wcp}	0.40	0.34	0.39	0.39
S_{or}	0.57	0.51	0.56	0.55

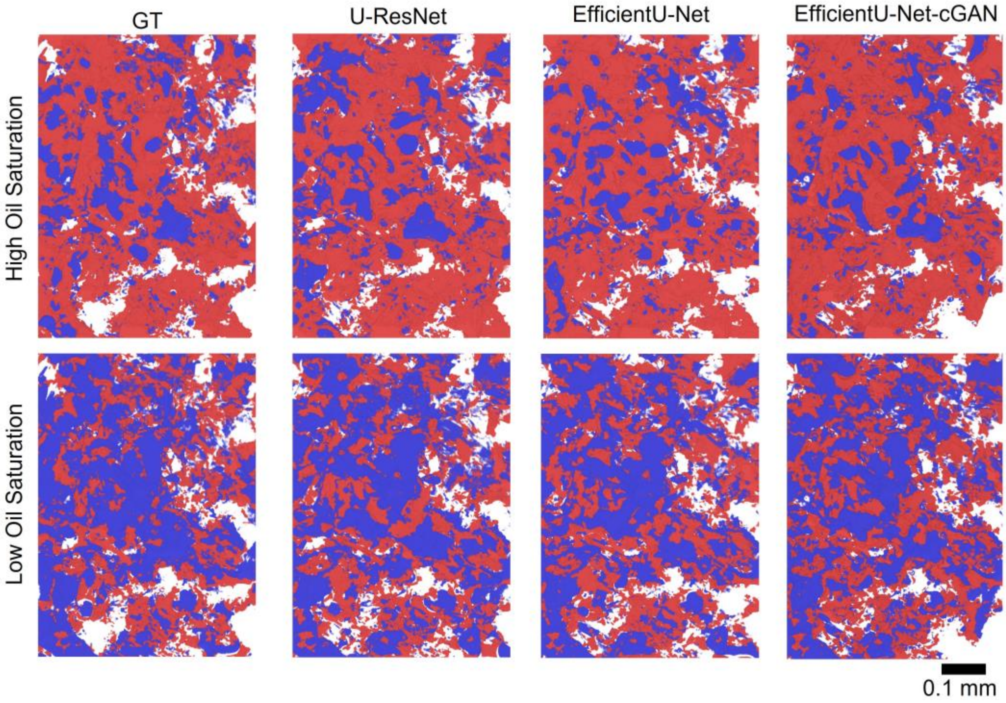

Figure 16: Visualization of the simulated domain from top to bottom at 1,001,000 LBM timesteps (high oil saturation) and 2,484,000 LBM timesteps (low oil saturation). The blue region corresponds to water and red to oil.

To summarize the overall performance of the four tested networks, Table 8 includes all the metrics that were used to evaluate the network performance. Only four commonly occurring phases are considered here because both the mica phase and mixed phase are rare. All networks have their own best metrics, e.g., EfficientU-Net-cGAN has a higher number of accurate metrics. However, the network selection should be based on the application they are designed for. For example, to capture the flow behavior ina clay coated sample (such as Mt. Simon sandstone) where the clay commonly exists in the pore, EfficientU-Net and U-ResNet might be more suitable, EfficientU-Net has a better clay phase segmentation as well as relative permeability while U-ResNet show a better clay connectivity and clay interface determination. If the sample contains insignificant clay in the pore (Bentheimer sandstone), EfficientU-Net-cGAN is a better choice that gives a better segmentation of pore phase. For mineral identification application, where the flow behavior is not essential, the EfficientU-Net-cGAN might be selected since it provides better segmentation result in the minerals apart from quartz. Additionally, if there is limited training data, to avoid overfitting, U-ResNet might be the best option, because the architecture is simpler than other three and has less training parameters (Table 2). When considering these metrics, it should also be considered that consistency in the processing workflow is of upmost importance, which is an attribute that all networks provide.

Table 8: Summary of accuracy measurements for the four networks. The symbol √ refers to the best result in terms of the given metric, while ○ refers to the second-best result. For those

networks that have only one acceptable result, only the best performance is ticked. EfficientU-Net-cGAN had the best overall performance, including five best-performance metrics and three second-best metrics.

	Overall Pixel Accuracy	Phase Pixel Accuracy Pore	Clay	Quartz	Feldspar	Relative Permeability
U-ResNet		○		○	○	
U-ResNet-cGAN		√		√		
EfficeintU-Net	√		√			√
EfficientUnet-cGAN	○		○		√	
	Euler Characteristic Pore	Clay	Quartz	Feldspar	Porosity	
U-ResNet		√	√			
U-ResNet-cGAN		○		√	√	
EfficeintU-Net	○				○	
EfficientUnet-cGAN	√		○			
	Region-based Accuracy Pore	Clay	Quartz	Feldspar	Absolute permeability	
U-ResNet		√	○	○		
U-ResNet-cGAN			√			
EfficientU-Net	○	○				
EfficientUnet-cGAN	√			√	√	

4 Conclusion

To perform multi-mineral segmentation on dynamic synchrotron-based images with a certain degree of noise associated with fast imaging, unpaired domain transfer was implemented using CycleGan. It performs unpaired domain transfers of synchrotron-based μ-CT data into raw μ-CT data with ground-truth labels. Dynamic-styled μ-CT data are further degraded by adding Poisson and Gaussian noises, which are the common noise in μ-CT imaging. Four deep-convolutional neural networks were used to segment the degraded synchrotron-style Mt. Simon sandstone images. The pixelwise accuracy for all networks converged to approximately 94%. The accuracy for EfficientU-Net and EfficientU-Net-cGAN was marginally better than that of U-ResNet and U-ResNet-cGAN. Physical accuracy was also determined to further compare the segmentation results of each network. The physical measurements of connectivity showed higher variance, especially in the less-common phases. All networks provided an accurate prediction in the volume-fraction measurement, with a maximum difference of less than 5%. EfficientU-Net-cGAN provided an accurate measurement of absolute permeability and yielded the best performance for interface segmentation, whereas EfficientU-Net provided an accurate prediction in terms of relative permeability simulations for mixed-wetting conditions. From the high pixelwise and physical accuracy, we demonstrate that the unpaired domain transfer by CycleGan can capture the semantic or style from an image and transfer into another image. It is helpful in reducing the quantity requirement of ground truth for semantic segmentation tasks.

With the integration of the dynamic-based image processing workflow of unpaired domain transfer and CNN methods, this research presents a application of real-time imaging and DRP for pore-scale CCS and UHS investigations. More specifically, the proposed image-processing workflow performs multi-mineral segmentation on a real-time image by transferring dynamic information from synchrotron-based scanning of a rock sample to a long-scanned, high-quality rock image without the requirement of real-time ground-truth data. A DRP with multiple phases can then be implemented with the validation of multiphase-flow experimental data generated during dynamic image scanning. The workflow is generalizable to studying any type of porous media with multiphases, flow, or transport. For example, it could be applied to H_2 diffusion experiments with dynamic scanning in order to understand the relationship between diffusion and rock mineralogy, as well as to mineral dissolution and precipitation or the development of gas pockets within a hydrogen fuel cell that reduces overall transport efficiencies [98].

In addition to the specific case described in this study, the workflow serves as a semi-automatic process for the image processing of porous materials. Traditionally, the μ-CT image is first subjected to several preprocessing steps such as filtering and pixel matching before segmentation, which requires a great amount of human effort, including human biases. By using the proposed workflow, an automatic "filtering" and "pixel matching" is implemented by unpaired domain transfer with CycleGAN, which is the major objective and contribution of the study. Domain transfer is then followed by an automatic multiphase segmentation without any human effort or bias. The objective is that training data and learning mappings from previous works can be applied to unseen works from completely different instruments and settings. Thus, the methodology allows for applying trained algorithms to a broad range of data in a consistent and objective way. A step toward the development of a fully automatic workflow is to couple the CycleGAN with the CNN segmentation networks into a single network; this requires a more complex network structure and hyperparameter tuning to balance the loss functions along with a means to dynamically adjust the learning rate. Meanwhile, additional image information could also help to increase the segmentation performance. This could be different image modalities or the same modality with different settings, such as dual energy images or phase contrast images. The overall workflow provides a digital material platform for the study of physical processes within complex porous structures containing multiphases that can deal with the noise associated with dynamic real-time imaging.

Acknowledgement

The authors acknowledge the Tyree X-ray CT Facility, a UNSW network lab funded by the UNSW Research Infrastructure Scheme, for the acquisition of the 3D micro-CT images. And this research used resources of the Advanced Photon Source, a U.S. Department of Energy (DOE) Office of Science User Facility operated for the DOE Office of Science by Argonne National Laboratory under Contract No. DE-AC02-06CH11357, for imaging synchrotron-based X-ray data.

Statement

All the data that support the findings of this study are available from the corresponding author upon reasonable request.

References

[1] R. S. Dimitrov, *The Paris Agreement on Climate Change: Behind Closed Doors*, Global Environmental Politics **16**, 1 (2016).

[2] J. Rogelj, M. den Elzen, N. Höhne, T. Fransen, H. Fekete, H. Winkler, R. Schaeffer, F. Sha, K. Riahi, and M. Meinshausen, *Paris Agreement Climate Proposals Need a Boost to Keep Warming Well below 2 ° C*, Nature **534**, 7609 (2016).

[3] S. N. Seo, *Beyond the Paris Agreement: Climate Change Policy Negotiations and Future Directions*, Regional Science Policy & Practice **9**, 121 (2017).

[4] P. O. Carden and L. Paterson, *Physical, Chemical and Energy Aspects of Underground Hydrogen Storage*, International Journal of Hydrogen Energy **4**, 559 (1979).

[5] K. Damen, A. Faaij, and W. Turkenburg, *Health, Safety and Environmental Risks of Underground Co2 Storage – Overview of Mechanisms and Current Knowledge*, Climatic Change **74**, 289 (2006).

[6] S. L'Orange Seigo, S. Dohle, and M. Siegrist, *Public Perception of Carbon Capture and Storage (CCS): A Review*, Renewable and Sustainable Energy Reviews **38**, 848 (2014).

[7] R. Tarkowski, *Underground Hydrogen Storage: Characteristics and Prospects*, Renewable and Sustainable Energy Reviews **105**, 86 (2019).

[8] A. Alhosani, Q. Lin, A. Scanziani, E. Andrews, K. Zhang, B. Bijeljic, and

M. J. Blunt, *Pore-Scale Characterization of Carbon Dioxide Storage at Immiscible and near-Miscible Conditions in Altered-Wettability Reservoir Rocks*, International Journal of Greenhouse Gas Control **105**, 103232 (2021).

[9] S. Krevor, M. J. Blunt, S. M. Benson, C. H. Pentland, C. Reynolds, A. Al-Menhali, and B. Niu, *Capillary Trapping for Geologic Carbon Dioxide Storage – From Pore Scale Physics to Field Scale Implications*, International Journal of Greenhouse Gas Control **40**, 221 (2015).

[10] S. Flesch, D. Pudlo, D. Albrecht, A. Jacob, and F. Enzmann, *Hydrogen Underground Storage—Petrographic and Petrophysical Variations in Reservoir Sandstones from Laboratory Experiments under Simulated Reservoir Conditions*, International Journal of Hydrogen Energy **43**, 20822 (2018).

[11] D. Zivar, S. Kumar, and J. Foroozesh, *Underground Hydrogen Storage: A Comprehensive Review*, International Journal of Hydrogen Energy (2020).

[12] Z. Bo, L. Zeng, Y. Chen, and Q. Xie, *Geochemical Reactions-Induced Hydrogen Loss during Underground Hydrogen Storage in Sandstone Reservoirs*, International Journal of Hydrogen Energy (2021).

[13] M. J. Blunt, B. Bijeljic, H. Dong, O. Gharbi, S. Iglauer, P. Mostaghimi, A. Paluszny, and C. Pentland, *Pore-Scale Imaging and Modelling*, Advances in Water Resources **51**, 197 (2013).

[14] P. Mostaghimi, R. T. Armstrong, A. Gerami, Y. Hu, Y. Jing, F. Kamali, M. Liu, Z. Liu, X. Lu, H. L. Ramandi, A. Zamani, and Y. Zhang, *Cleat-Scale Characterisation of Coal: An Overview*, Journal of Natural Gas Science and Engineering **39**, 143 (2017).

[15] Y. D. Wang, M. J. Blunt, R. T. Armstrong, and P. Mostaghimi, *Deep Learning in Pore Scale Imaging and Modeling*, Earth-Science Reviews **215**, 103555 (2021).

[16] A. Kääb and M. Vollmer, *Surface Geometry, Thickness Changes and Flow Fields on Creeping Mountain Permafrost: Automatic Extraction by Digital Image Analysis*, Permafrost and Periglacial Processes **11**, 315 (2000).

[17] M. A. Knackstedt, S. Latham, M. Madadi, A. Sheppard, T. Varslot, and C. Arns, *Digital Rock Physics: 3D Imaging of Core Material and Correlations to Acoustic and Flow Properties*, The Leading Edge **28**, 28 (2009).

[18] H. Andrä, N. Combaret, J. Dvorkin, E. Glatt, J. Han, M. Kabel, Y. Keehm, F. Krzikalla, M. Lee, C. Madonna, M. Marsh, T. Mukerji, E. H. Saenger, R. Sain, N. Saxena, S. Ricker, A. Wiegmann, and X. Zhan, *Digital Rock Physics Benchmarks—Part I: Imaging and Segmentation*, Computers & Geosciences **50**, 25 (2013).

[19] I. Verri, A. Della Torre, G. Montenegro, A. Onorati, S. Duca, C. A. Mora, F. Radaelli, and G. Trombin, *Development of a Digital Rock Physics Workflow for the Analysis of Sandstones and Tight Rocks*, Journal of Petroleum Science and Engineering **156**, 790 (2017).

[20] S. Berg, H. Ott, S. A. Klapp, A. Schwing, R. Neiteler, N. Brussee, A. Makurat, L. Leu, F. Enzmann, J.-O. Schwarz, M. Kersten, S. Irvine, and M. Stampanoni, *Real-Time 3D Imaging of Haines Jumps in Porous Media Flow*, PNAS **110**, 3755 (2013).

[21] T. Bultreys, M. A. Boone, M. N. Boone, T. De Schryver, B. Masschaele, L. Van Hoorebeke, and V. Cnudde, *Fast Laboratory-Based Micro-Computed Tomography for Pore-Scale Research: Illustrative Experiments and Perspectives on the Future*, Advances in Water Resources **95**, 341 (2016).
[22] G. Dalen and M. Koster, *2D & 3D Particle Size Analysis of Micro-CT Images*, in (2012).
[23] Y. Jing, R. T. Armstrong, and P. Mostaghimi, *Image-Based Fracture Pipe Network Modelling for Prediction of Coal Permeability*, Fuel **270**, 117447 (2020).
[24] S. Karimpouli, P. Tahmasebi, H. L. Ramandi, P. Mostaghimi, and M. Saadatfar, *Stochastic Modeling of Coal Fracture Network by Direct Use of Micro-Computed Tomography Images*, International Journal of Coal Geology **179**, 153 (2017).
[25] F. Reyes, Q. Lin, O. Udoudo, C. Dodds, P. D. Lee, and S. J. Neethling, *Calibrated X-Ray Micro-Tomography for Mineral Ore Quantification*, Minerals Engineering **110**, 122 (2017).
[26] M. Liu, M. Shabaninejad, and P. Mostaghimi, *Predictions of Permeability, Surface Area and Average Dissolution Rate during Reactive Transport in Multi-Mineral Rocks*, Journal of Petroleum Science and Engineering **170**, 130 (2018).
[27] Y. D. Wang, T. Chung, R. T. Armstrong, J. McClure, T. Ramstad, and P. Mostaghimi, *Accelerated Computation of Relative Permeability by Coupled Morphological and Direct Multiphase Flow Simulation*, Journal of Computational Physics **401**, 108966 (2020).
[28] T. Akai, A. M. Alhammadi, M. J. Blunt, and B. Bijeljic, *Modeling Oil Recovery in Mixed-Wet Rocks: Pore-Scale Comparison Between Experiment and Simulation*, Transp Porous Med **127**, 393 (2019).
[29] C. H. Arns, M. A. Knackstedt, W. V. Pinczewski, and K. R. Mecke, *Euler-Poincar\' e Characteristics of Classes of Disordered Media*, Phys. Rev. E **63**, 031112 (2001).
[30] C. Madonna, B. S. G. Almqvist, and E. H. Saenger, *Digital Rock Physics: Numerical Prediction of Pressure-Dependent Ultrasonic Velocities Using Micro-CT Imaging*, Geophysical Journal International **189**, 1475 (2012).
[31] A. Narváez, T. Zauner, F. Raischel, R. Hilfer, and J. Harting, *Quantitative Analysis of Numerical Estimates for the Permeability of Porous Media from Lattice-Boltzmann Simulations*, J. Stat. Mech. **2010**, P11026 (2010).
[32] Y. A. Alzahid, H. Aborshaid, M. Asali, J. McClure, C. Chen, P. Mostaghimi, Y. Da Wang, C. Sun, and R. T. Armstrong, *Real-Time Synchrotron-Based X-Ray Computed Microtomography during in Situ Emulsification*, Journal of Petroleum Science and Engineering **195**, 107885 (2020).
[33] D. Wildenschild and A. P. Sheppard, *X-Ray Imaging and Analysis Techniques for Quantifying Pore-Scale Structure and Processes in Subsurface Porous Medium Systems*, Advances in Water Resources **51**, 217 (2013).
[34] R. T. Armstrong, N. Evseev, D. Koroteev, and S. Berg, *Modeling the Velocity Field during Haines Jumps in Porous Media*, Advances in Water Resources **77**,

57 (2015).

[35] C. Madonna, B. Quintal, M. Frehner, B. S. G. Almqvist, N. Tisato, M. Pistone, F. Marone, and E. H. Saenger, *Synchrotron-Based X-Ray Tomographic Microscopy for Rock Physics Investigations*, Geophysics **78**, D53 (2013).

[36] M. Heyndrickx, T. Bultreys, W. Goethals, L. Van Hoorebeke, and M. N. Boone, *Improving Image Quality in Fast, Time-Resolved Micro-CT by Weighted Back Projection*, Scientific Reports **10**, 1 (2020).

[37] Y. Da Wang, M. Shabaninejad, R. T. Armstrong, and P. Mostaghimi, *Physical Accuracy of Deep Neural Networks for 2D and 3D Multi-Mineral Segmentation of Rock Micro-CT Images*, ArXiv:2002.05322 [Cs, Eess] (2020).

[38] S. Karimpouli and P. Tahmasebi, *Segmentation of Digital Rock Images Using Deep Convolutional Autoencoder Networks*, Computers & Geosciences **126**, 142 (2019).

[39] Y. Niu, P. Mostaghimi, M. Shabaninejad, P. Swietojanski, and R. T. Armstrong, *Digital Rock Segmentation for Petrophysical Analysis With Reduced User Bias Using Convolutional Neural Networks*, Water Resources Research **56**, e2019WR026597 (2020).

[40] O. Sudakov, E. Burnaev, and D. Koroteev, *Driving Digital Rock towards Machine Learning: Predicting Permeability with Gradient Boosting and Deep Neural Networks*, Computers & Geosciences **127**, 91 (2019).

[41] D. Tang and K. Spikes, *Segmentation of Shale SEM Images Using Machine Learning*, in *SEG Technical Program Expanded Abstracts 2017* (Society of Exploration Geophysicists, 2017), pp. 3898–3902.

[42] R. Girshick, J. Donahue, T. Darrell, and J. Malik, *Rich Feature Hierarchies for Accurate Object Detection and Semantic Segmentation*, (2013).

[43] K. He, X. Zhang, S. Ren, and J. Sun, *Deep Residual Learning for Image Recognition*, (2015).

[44] M. Tan and Q. V. Le, *EfficientNet: Rethinking Model Scaling for Convolutional Neural Networks*, ArXiv:1905.11946 [Cs, Stat] (2020).

[45] C. Dong, C. C. Loy, K. He, and X. Tang, *Image Super-Resolution Using Deep Convolutional Networks*, ArXiv:1501.00092 [Cs] (2015).

[46] P. Isola, J.-Y. Zhu, T. Zhou, and A. A. Efros, *Image-to-Image Translation with Conditional Adversarial Networks*, ArXiv:1611.07004 [Cs] (2018).

[47] K. He, G. Gkioxari, P. Dollár, and R. Girshick, *Mask R-CNN*, ArXiv:1703.06870 [Cs] (2018).

[48] O. Ronneberger, P. Fischer, and T. Brox, *U-Net: Convolutional Networks for Biomedical Image Segmentation*, ArXiv:1505.04597 [Cs] (2015).

[49] H. P. Narkhede, *Review of Image Segmentation Techniques*, **1**, 8 (2013).

[50] J. Kuruvilla, D. Sukumaran, A. Sankar, and S. P. Joy, *A Review on Image Processing and Image Segmentation*, in *2016 International Conference on Data Mining and Advanced Computing (SAPIENCE)* (2016), pp. 198–203.

[51] S. Rubaiya Muin, P. T. Spicer, K. Tang, Y. Niu, M. Hosseini, P. Mostaghimi, and R. T. Armstrong, *Dynamic X-Ray Micotomography of Microfibrous Cellulose Liquid Foams Using Deep Learning*, Chemical Engineering Science **248**, 117173

(2022).
[52] H. Zhu, F. Meng, J. Cai, and S. Lu, *Beyond Pixels: A Comprehensive Survey from Bottom-up to Semantic Image Segmentation and Cosegmentation*, Journal of Visual Communication and Image Representation **34**, 12 (2016).
[53] T. Zhou, S. Ruan, and S. Canu, *A Review: Deep Learning for Medical Image Segmentation Using Multi-Modality Fusion*, Array **3–4**, 100004 (2019).
[54] S. Hao, Y. Zhou, and Y. Guo, *A Brief Survey on Semantic Segmentation with Deep Learning*, Neurocomputing **406**, 302 (2020).
[55] P. Gravel, G. Beaudoin, and J. A. DeGuise, *A Method for Modeling Noise in Medical Images*, IEEE Trans. Med. Imaging **23**, 1221 (2004).
[56] I. Ar Rushood, N. Alqahtani, Y. D. Wang, M. Shabaninejad, R. Armstrong, and P. Mostaghimi, *Segmentation of X-Ray Images of Rocks Using Deep Learning*, in (Society of Petroleum Engineers, 2020).
[57] N. Srisutthiyakorn*, *Deep-Learning Methods for Predicting Permeability from 2D/3D Binary-Segmented Images*, in *SEG Technical Program Expanded Abstracts 2016* (Society of Exploration Geophysicists, 2016), pp. 3042–3046.
[58] M. Fan, J. E. McClure, R. T. Armstrong, M. Shabaninejad, L. E. Dalton, D. Crandall, and C. Chen, *Influence of Clay Wettability Alteration on Relative Permeability*, Geophysical Research Letters **47**, e2020GL088545 (2020).
[59] M. Liu, M. Shabaninejad, and P. Mostaghimi, *Impact of Mineralogical Heterogeneity on Reactive Transport Modelling*, Computers & Geosciences **104**, 12 (2017).
[60] T.-Y. Lin, P. Goyal, R. Girshick, K. He, and P. Dollár, *Focal Loss for Dense Object Detection*, ArXiv:1708.02002 [Cs] (2018).
[61] V. Davidoiu, L. Hadjilucas, I. Teh, N. P. Smith, J. E. Schneider, and J. Lee, *Evaluation of Noise Removal Algorithms for Imaging and Reconstruction of Vascular Networks Using Micro-CT*, Biomed. Phys. Eng. Express **2**, 045015 (2016).
[62] M. Tuller, R. Kulkarni, and W. Fink, *Segmentation of X-Ray CT Data of Porous Materials: A Review of Global and Locally Adaptive Algorithms*, in *Soil-Water-Root Processes: Advances in Tomography and Imaging,* Vol. 61 (2013), pp. 157–182.
[63] J. Wang, H. Lu, Z. Liang, D. Eremina, G. Zhang, S. Wang, J. Chen, and J. Manzione, *An Experimental Study on the Noise Properties of X-Ray CT Sinogram Data in Radon Space*, Phys Med Biol **53**, 3327 (2008).
[64] H. Zhang, D. Zeng, H. Zhang, J. Wang, Z. Liang, and J. Ma, *Applications of Nonlocal Means Algorithm in Low-Dose X-Ray CT Image Processing and Reconstruction: A Review*, Med Phys **44**, 1168 (2017).
[65] P. I. Guntoro, Y. Ghorbani, P.-H. Koch, and J. Rosenkranz, *X-Ray Microcomputed Tomography (MCT) for Mineral Characterization: A Review of Data Analysis Methods*, Minerals **9**, 3 (2019).
[66] M. Balafar, *Review of Noise Reducing Algorithms for Brain MRI Images*, Ijtpe **4**, 54 (2012).
[67] Y. Wang, S. Basu, and C.-Y. Wang, *Modeling Two-Phase Flow in PEM Fuel Cell*

Channels, Journal of Power Sources **179**, 603 (2008).

[68] A. Anagnostopoulos, S. Knauer, Y. Ding, and Y. Grosu, *Giant Effect of Negative Compressibility in a Water - Porous Metal - CO2 System for Sensing Applications*, ACS Appl. Mater. Interfaces **12**, 39756 (2020).

[69] A. Lowe, N. Tsyrin, M. Chorążewski, P. Zajdel, M. Mierzwa, J. B. Leão, M. Bleuel, T. Feng, D. Luo, M. Li, D. Li, V. Stoudenets, S. Pawlus, A. Faik, and Y. Grosu, *Effect of Flexibility and Nanotriboelectrification on the Dynamic Reversibility of Water Intrusion into Nanopores: Pressure-Transmitting Fluid with Frequency-Dependent Dissipation Capability*, ACS Appl. Mater. Interfaces **11**, 40842 (2019).

[70] Y. Grosu, Y. Zhao, A. Giacomello, S. Meloni, J.-L. Dauvergne, A. Nikulin, E. Palomo, Y. Ding, and A. Faik, *Hierarchical Macro-Nanoporous Metals for Leakage-Free High-Thermal Conductivity Shape-Stabilized Phase Change Materials*, Applied Energy **269**, 115088 (2020).

[71] J.-Y. Zhu, T. Park, P. Isola, and A. A. Efros, *Unpaired Image-to-Image Translation Using Cycle-Consistent Adversarial Networks*, (2017).

[72] J. E. Elkhoury, R. Shankar, and T. S. Ramakrishnan, *Resolution and Limitations of X-Ray Micro-CT with Applications to Sandstones and Limestones*, Transp Porous Med **129**, 413 (2019).

[73] R. T. Armstrong, C. Sun, P. Mostaghimi, S. Berg, M. Rücker, P. Luckham, A. Georgiadis, and J. E. McClure, *Multiscale Characterization of Wettability in Porous Media*, Transp Porous Med **140**, 215 (2021).

[74] R. Huang, A. L. Herring, and A. Sheppard, *Effect of Saturation and Image Resolution on Representative Elementary Volume and Topological Quantification: An Experimental Study on Bentheimer Sandstone Using Micro-CT*, Transp Porous Med **137**, 489 (2021).

[75] Z. Wojna, V. Ferrari, S. Guadarrama, N. Silberman, L.-C. Chen, A. Fathi, and J. Uijlings, *The Devil Is in the Decoder: Classification, Regression and GANs*, ArXiv:1707.05847 [Cs] (2019).

[76] D. Ulyanov, A. Vedaldi, and V. Lempitsky, *Instance Normalization: The Missing Ingredient for Fast Stylization*, ArXiv:1607.08022 [Cs] (2017).

[77] A. G. Howard, M. Zhu, B. Chen, D. Kalenichenko, W. Wang, T. Weyand, M. Andreetto, and H. Adam, *MobileNets: Efficient Convolutional Neural Networks for Mobile Vision Applications*, ArXiv:1704.04861 [Cs] (2017).

[78] J. Bear, *Dynamics of Fluids in Porous Media* (Courier Corporation, 1988).

[79] K. Xi, Y. Cao, K. Liu, J. Jahren, R. Zhu, G. Yuan, and H. Hellevang, *Authigenic Minerals Related to Wettability and Their Impacts on Oil Accumulation in Tight Sandstone Reservoirs: An Example from the Lower Cretaceous Quantou Formation in the Southern Songliao Basin, China*, Journal of Asian Earth Sciences **178**, 173 (2019).

[80] J. E. McClure, Z. Li, M. Berrill, and T. Ramstad, *The LBPM Software Package for Simulating Multiphase Flow on Digital Images of Porous Rocks*, ArXiv:2007.12266 [Physics] (2020).

[81] T. Chung, Y. D. Wang, R. T. Armstrong, and P. Mostaghimi, *Approximating*

Permeability of Microcomputed-Tomography Images Using Elliptic Flow Equations, SPE Journal **24**, 1,154 (2019).

[82] Y. D. Wang, T. Chung, R. Armstrong, J. Mcclure, and P. Mostaghimi, *Computations of Permeability of Large Rock Images by Dual Grid Domain Decomposition*, Advances in Water Resources **126**, (2019).

[83] Y. D. Wang, T. Chung, A. Rabbani, R. T. Armstrong, and P. Mostaghimi, *Fast Direct Flow Simulation in Porous Media by Coupling with Pore Network and Laplace Models*, Advances in Water Resources **150**, 103883 (2021).

[84] M. Latva-Kokko and D. H. Rothman, *Scaling of Dynamic Contact Angles in a Lattice-Boltzmann Model*, Phys. Rev. Lett. **98**, 254503 (2007).

[85] A. Mittal, R. Soundararajan, and A. C. Bovik, *Making a "Completely Blind" Image Quality Analyzer*, IEEE Signal Processing Letters **20**, 209 (2013).

[86] A. Mittal, A. K. Moorthy, and A. C. Bovik, *No-Reference Image Quality Assessment in the Spatial Domain*, IEEE Transactions on Image Processing **21**, 4695 (2012).

[87] K. Singh, H. Menke, M. Andrew, C. Rau, B. Bijeljic, and M. J. Blunt, *Time-Resolved Synchrotron X-Ray Micro-Tomography Datasets of Drainage and Imbibition in Carbonate Rocks*, Sci Data **5**, (2018).

[88] M. Rücker, S. Berg, R. T. Armstrong, A. Georgiadis, H. Ott, A. Schwing, R. Neiteler, N. Brussee, A. Makurat, L. Leu, M. Wolf, F. Khan, F. Enzmann, and M. Kersten, *From Connected Pathway Flow to Ganglion Dynamics*, Geophysical Research Letters **42**, 3888 (2015).

[89] A. P. Sheppard, R. M. Sok, and H. Averdunk, *Techniques for Image Enhancement and Segmentation of Tomographic Images of Porous Materials*, Physica A: Statistical Mechanics and Its Applications **339**, 145 (2004).

[90] Y. Bazaikin, B. Gurevich, S. Iglauer, T. Khachkova, D. Kolyukhin, M. Lebedev, V. Lisitsa, and G. Reshetova, *Effect of CT Image Size and Resolution on the Accuracy of Rock Property Estimates*, Journal of Geophysical Research: Solid Earth **122**, 3635 (2017).

[91] L. Leu, S. Berg, F. Enzmann, R. T. Armstrong, and M. Kersten, *Fast X-Ray Micro-Tomography of Multiphase Flow in Berea Sandstone: A Sensitivity Study on Image Processing*, Transp Porous Med **105**, 451 (2014).

[92] R. T. Armstrong, J. E. McClure, V. Robins, Z. Liu, C. H. Arns, S. Schlüter, and S. Berg, *Porous Media Characterization Using Minkowski Functionals: Theories, Applications and Future Directions*, Transp Porous Med **130**, 305 (2019).

[93] Z. Jiang, K. Wu, G. D. Couples, and J. Ma, *The Impact of Pore Size and Pore Connectivity on Single-Phase Fluid Flow in Porous Media*, Advanced Engineering Materials **13**, 208 (2011).

[94] L. E. Treiber and W. W. Owens, *A Laboratory Evaluation of the Wettability of Fifty Oil-Producing Reservoirs*, Society of Petroleum Engineers Journal **12**, 531 (1972).

[95] C. A. Fauziah, E. A. Al-Khdheeawi, A. Barifcani, and S. Iglauer, *Wettability Measurements of Mixed Clay Minerals at Elevated Temperature and Pressure:*

Implications for CO2 Geo-Storage, in (OnePetro, 2019).

[96] B. Pan, X. Yin, and S. Iglauer, *A Review on Clay Wettability: From Experimental Investigations to Molecular Dynamics Simulations*, Adv Colloid Interface Sci **285**, 102266 (2020).

[97] L. W. Lake, *Enhanced Oil Recovery*, (1989).

[98] P. P. Edwards, V. L. Kuznetsov, W. I. F. David, and N. P. Brandon, *Hydrogen and Fuel Cells: Towards a Sustainable Energy Future*, Energy Policy **36**, 4356 (2008).